

# Monsoon depression amplification by moist barotropic instability in a vertically sheared environment

Michael Diaz<sup>1</sup>  | William R. Boos<sup>1,2</sup> 

<sup>1</sup>Department of Earth and Planetary Science, University of California, Berkeley, Berkeley, California

<sup>2</sup>Climate and Ecosystem Sciences Division, Lawrence Berkeley National Laboratory, Berkeley, California

## Correspondence

Michael Diaz, Department of Earth and Planetary Science, University of California, Berkeley, 307 McCone Hall, Berkeley, CA 94720-4767.

Email: mldiaz@ncsu.edu

## Funding information

U.S. Department of Energy, Office of Science, Biological and Environmental Research award DE-SC0019367, and National Science Foundation award AGS-1746160

## Abstract

This study makes the case that monsoon depressions over South Asia can form from a variant of moist barotropic instability. Using an idealized numerical framework in which the atmosphere is partitioned into a basic state and a perturbation, we simulate vortices resembling monsoon depressions that draw energy from the meridional shear of the monsoon trough and amplify when they interact with precipitating ascent. The influence of the basic state vertical shear on the vortex induces upward velocity, which couples precipitation with a Rossby-wave-like mode arising from dry barotropic growth, allowing the vortex to intensify. Sensitivity experiments reveal that both the sheared basic state and latent heating are necessary to achieve positive growth rates and that this process requires a sufficiently large initial perturbation. Trajectory analyses suggest that the combined flow of the vortex and the large-scale monsoon transport diabatically generated potential vorticity from southwest of the vortex into the vortex center, thus enabling growth. In contrast with tropical cyclones, this mechanism does not require a feedback between surface wind speed and surface heat and moisture fluxes, though this feedback does ultimately result in a slightly stronger vortex.

## KEYWORDS

barotropic instability, idealized numerical modeling, Indian Monsoon, monsoon depression, monsoon low-pressure system

## 1 | INTRODUCTION

Condensational heating from cumulus convection has long been recognized as the primary energy source for the growth of monsoon depressions in the Bay of Bengal (Krishnamurti *et al.*, 1976; Shukla, 1978). However, the mechanism that couples this convection to a depression-scale vortex and allows it to grow is less well understood. On its own, convection operates on a much smaller time and space scale compared with a monsoon depression. Thus, the challenge has been to find a mechanism that can organize convection on a larger scale, so that its energy can be used to foster the growth of a depression-scale vortex. A number of ideas have been discussed in past studies that warrant consideration.

One candidate is conditional instability of the second kind (CISK). There are two categories of CISK: one in which convection is organized by moisture convergence induced by boundary-layer friction (Charney and Eliassen, 1964) and another in which this moisture convergence is linked to an internal wave mode (Lindzen, 1974). Though Shukla (1978) carried out perhaps the only study devoted to monsoon depressions that has applied this theory quantitatively, many others have employed the concept qualitatively to explain some aspect of monsoon depressions (Chen and Yoon, 2000; Dash *et al.*, 2004; Chen *et al.*, 2005; Sørland *et al.*, 2016) or have speculated it to be important based on their results (Keshavamurty *et al.*, 1978; Goswami *et al.*, 1980; Sørland and Sorteberg, 2015). One nagging defect of CISK is that

it predicts maximum growth rates at the smallest resolvable scales (e.g., Crum and Dunkerton, 1992) and this flaw persists when applied to monsoon depressions (Shukla, 1978). Additionally, most wave-CISK theories are based on highly simplistic parametrizations of moist convection and classical wave-CISK modes do not appear in either observations or cloud-resolving numerical simulations (Bretherton, 2003).

Another possibility is that monsoon depressions amplify by a mechanism similar to that of tropical cyclones. The most widely accepted theory for tropical cyclone intensification is wind-induced surface heat exchange (WISHE), a process by which convection is organized by wind-speed-dependent surface heat and moisture fluxes (Emanuel, 1986; Rotunno and Emanuel, 1987). From a weather forecasting perspective, tropical cyclones are perhaps the closest analogue to monsoon depressions, with the Indian Meteorological Department (IMD) ranking weather systems in the Indian Ocean on a continuum which includes lows, depressions, and cyclonic storms. Storms within the last of those categories are equivalent to tropical cyclones and are given official names. Additionally, because of similarities between environmental conditions favoring monsoon depressions (Sikka, 1977) and those favoring tropical cyclones, some studies have used the genesis potential index (GPI) developed for tropical cyclones (Emanuel and Nolan, 2004) to explain long-term trends in monsoon depression frequency (Prajeesh *et al.*, 2013; Vishnu *et al.*, 2016; 2018). Parameters included in the GPI, such as vertical wind shear, sea-surface temperature, absolute vorticity, and relative humidity, are also frequently discussed in IMD bulletins providing forecasts for monsoon depressions. Despite these similarities, one curious discrepancy is that monsoon depressions often form in an environment of high vertical wind shear. In fact, because of this shear, the GPI predicts conditions over the Bay of Bengal to be less favorable for tropical cyclogenesis during the middle of summer (Camargo *et al.*, 2007; Tippett *et al.*, 2011), a time when monsoon depression frequency peaks (Hurley and Boos, 2015; Ditchek *et al.*, 2016). Whether they form because of this shear, or in spite of it, is not clear. Additionally, monsoon depressions occasionally form over land, where the GPI is undefined, since it requires a value for sea-surface temperature. Both of these observations suggest that monsoon depressions may be a phenomenon distinct from tropical cyclones.

Though generally detrimental to tropical cyclone intensification, vertical shear could promote other growth mechanisms. Unlike most of the maritime Tropics, the South Asian monsoon features a strong time-mean meridional temperature gradient, which is in approximate thermal wind balance with its strong vertical shear. This peculiarity has led many to argue that monsoon depressions are a manifestation of moist baroclinic instability (Moorthi and Arakawa, 1985; Krishnakumar *et al.*, 1992; Kasture *et al.*, 1993; Aravequia *et al.*,

1995; Krishnamurti *et al.*, 2013). In this theory, precipitation is organized by a synoptic-scale baroclinic wave, the warm advection of which drives ascent and condensation. When this condensation is biased into the warm part of the wave, instead of remaining strictly in quadrature, it enhances the growth of the original baroclinic wave. A major problem with this mechanism as an explanation for monsoon depressions is that it requires a growing disturbance to tilt upshear (Cohen and Boos, 2016). Monsoon depressions, by contrast, generally exhibit no tilt or a slightly downshear tilt (Keshavamurty *et al.*, 1978; Cohen and Boos, 2016).

In addition to a strong meridional temperature gradient, the South Asian monsoon also exhibits a substantial meridional gradient of moisture. Adames and Ming (2018a) argue that this juxtaposition could lead to growing depression-scale disturbances through a process they have termed moisture-vortex instability, which is an extension of the moisture mode theory of Sobel *et al.* (2001). According to this idea, convection is organized by the advection of warm air and moisture in the northerly flow to the west of the vortex. This convection in turn amplifies the vortex through vorticity stretching. A necessary feature for growth in this mechanism is a time delay between the peak moistening rate and convection, which shifts the vortex stretching into phase with the positive vorticity. A problem with this mechanism in regards to monsoon depressions is that it requires the ascent driven by meridional temperature advection to be weak compared with the ascent driven by meridional moisture advection, a circumstance in disagreement with the presence of a strong temperature gradient and the results of Adames and Ming (2018b).

Another prominent feature of the South Asian monsoon is a strong meridional gradient of vorticity. Various studies have noted that this gradient can sometimes reverse sign, leading to the potential for barotropic instability, with the meridional shear serving as an energy source (Krishnamurti *et al.*, 1976; Keshavamurty *et al.*, 1978; Goswami *et al.*, 1980; Nitta and Masuda, 1981; Subrahmanyam *et al.*, 1981; Lindzen *et al.*, 1983; Mishra, 2018). Recently, Diaz and Boos (2019) provided additional evidence to support this idea: a normal-mode linear instability analysis of a basic state representative of the environment preceding monsoon depression genesis over the Bay of Bengal yielded wave structures resembling monsoon depressions, the primary energy source of which was the basic-state meridional shear. However, they also found that, although zonally symmetric basic states were unstable, a basic state with realistic zonal variations was not. In this latter case, although wave structures were isolated that drew energy from the meridional shear and resembled monsoon depressions, energy lost to dissipative processes led to the net growth rate being weakly negative. Nevertheless, they noted that these wave structures had regions of upward vertical velocity, which they speculated could couple them to convection and lead to

positive net growth. Building upon the results of Diaz and Boos (2019), the goal of this study is to test that speculation. In other words, are monsoon depressions a variant of moist barotropic instability?

This study is outlined as follows. In section 2, we introduce the numerical modeling framework. We present the structure and energetics of the disturbance for the control simulation in section 3.1 and then discuss how it interacts with moist convection in section 3.2. In section 3.3, we present sensitivity experiments to gain further insight into which physical processes are important, including assessing to what extent the WISHE and frictional CISK mechanisms are applicable. Finally, in section 4, we summarize the results.

## 2 | METHODS

We use the same numerical modeling framework developed in Diaz and Boos (2019) as a starting point. In that study, we took the anelastic equations for atmospheric flow and derived a new equation set that is partitioned into a basic state and a perturbation. This partitioning provides a conceptually simpler interpretation of how a disturbance interacts with a specified background flow compared with solving the unpartitioned equation set. In the present study, we will augment this equation set to include representations of moist convection, turbulence, and surface fluxes.

### 2.1 | Governing equations

The momentum, heat, and pressure fields are governed by the following equations:

$$\frac{\partial \mathbf{u}'}{\partial t} = -(\bar{\mathbf{U}} + \mathbf{u}') \cdot \nabla \mathbf{u}' - \mathbf{u}' \cdot \nabla \bar{\mathbf{U}} - \nabla \phi' + b' \hat{\mathbf{k}} - f \hat{\mathbf{k}} \times \mathbf{v}' + \mathbf{T}'_{\mathbf{u}}, \quad (1a)$$

$$\frac{\partial \theta'}{\partial t} = -(\bar{\mathbf{U}} + \mathbf{u}') \cdot \nabla \theta' - \mathbf{u}' \cdot \nabla \bar{\theta} - w' \frac{d\theta_0}{dz} + M'_\theta + T'_\theta, \quad (1b)$$

$$\frac{\partial^2 \phi'}{\partial x^2} + \frac{\partial^2 \phi'}{\partial y^2} + \frac{\partial}{\partial z} \left( \rho_0 \frac{\partial \phi'}{\partial z} \right) = \nabla \cdot (\rho_0 G \{ \mathbf{u}' \}) \quad (1c)$$

where  $\mathbf{u} = \langle u, v, w \rangle$  represents the three-dimensional velocity field,  $\mathbf{v} = \langle u, v, 0 \rangle$  the horizontal velocity field,  $\theta$  is the potential temperature,  $\rho_0$  is the base state density, and  $\phi$  is the pressure variable, defined as  $\phi \equiv p/\rho_0$ , with  $p$  being standard pressure. The primes denote perturbation values and bars basic-state values. As is commonly done in anelastic systems, the basic-state potential temperature is partitioned into a horizontally uniform part,  $\theta_0$ , and a horizontally varying part,  $\bar{\theta}$ . Microphysical processes, that is, condensation and evaporation, are represented by  $M$  and tendencies from surface fluxes and subgrid-scale turbulence by  $T$ . The buoyancy term ( $b'$ ) is

defined in terms of virtual potential temperature,

$$b' = g \left( \frac{\theta'}{\theta_0} + 0.61q' - c - r \right), \quad (2)$$

where  $q'$  is the perturbation water-vapor mixing ratio,  $c$  is the cloud-water mixing ratio, and  $r$  is the rain-water mixing ratio. These moisture variables obey the following equations:

$$\frac{\partial q'}{\partial t} = -(\bar{\mathbf{U}} + \mathbf{u}') \cdot \nabla q' - \mathbf{u}' \cdot \nabla \bar{q} - w' \frac{dq_0}{dz} + M'_q + T'_q, \quad (3a)$$

$$\frac{\partial c}{\partial t} = -(\bar{\mathbf{U}} + \mathbf{u}') \cdot \nabla c + M_c + T_c, \quad (3b)$$

$$\frac{\partial r}{\partial t} = -(\bar{\mathbf{U}} + \mathbf{u}') \cdot \nabla r - w_t \frac{\partial r}{\partial z} + M_r + T_r, \quad (3c)$$

where  $w_t$  is the terminal velocity of rain, and  $M$  and  $T$  represent sources and sinks of each moisture variable due to microphysical processes and subgrid-scale turbulence, respectively. The equation for water vapor ( $q$ ) is derived in the same manner as that for  $\theta$ . By contrast, cloud and rain water do not have a basic state. This formulation is equivalent to neglecting advection of the basic-state cloud and rain field. The microphysics tendencies are calculated using a Kessler microphysics scheme (Kessler, 1969), which includes only warm rain processes.

### 2.2 | Surface heat and momentum fluxes

Since it is possible that monsoon depressions draw energy through a WISHE-like or a CISK-like process, and because frictional dissipation can be a large sink of energy, it is important to have a representation of surface fluxes of heat, moisture, and momentum. With the existence of a time-independent basic state, special consideration must be given to their formulation. We assume that the basic-state temperature, moisture, and wind distributions are in equilibrium with their respective basic-state surface fluxes, such that, when added to Equation 1, these fluxes preserve the time independence of the basic state. The perturbation flux for a generic scalar variable  $a$  can be defined as

$$F'_a = F_a - \bar{F}_a. \quad (4)$$

The total flux can be parametrized as

$$F_a = C_E |\mathbf{v}_{z_0}| (a_s - a_{z_0}), \quad (5)$$

where  $a_{z_0}$  is the value of  $a$  at the lowest model level,  $a_s$  is its surface value,  $|\mathbf{v}_{z_0}|$  is the wind speed at the lowest model level, and  $C_E$  is a non-dimensional drag or exchange coefficient. Partitioning all variables into their basic-state and perturbation values and substituting into Equations 5 and 4 yields the

perturbation surface latent and sensible heat fluxes,

$$F'_q = C_E \left\{ (|\mathbf{v}| - |\bar{\mathbf{V}}|) (q_s^* - \bar{q} - q_0) - |\mathbf{v}| q' \right\}_{z_0}, \quad (6a)$$

$$F'_\theta = C_E \left\{ (|\mathbf{v}| - |\bar{\mathbf{V}}|) (T_s - \bar{T}) - |\mathbf{v}| \theta' \right\}_{z_0}, \quad (6b)$$

where  $q_s^*$  is the saturation mixing ratio at the ocean surface,  $T_s$  the surface temperature of the ocean, and  $\bar{T}$  the basic-state surface air temperature. All quantities except for  $q_s^*$  and  $T_s$  are evaluated at the lowest model level ( $z_0$ ). One interpretation of Equation 6a is that anomalous positive moisture fluxes occur in regions where the near-surface air is anomalously cool or dry or where the near-surface wind speed exceeds its basic-state value. Following Rotunno and Emanuel (1987),  $C_E$  is set to

$$C_E = 1.1 \times 10^{-3} + 4 \times 10^{-5} |\mathbf{v}_{z_0}| \quad (7)$$

over the ocean. Over land,  $F'_q$  and  $F'_\theta$  are set to zero. Note that although these perturbation fluxes are zero over land, there are still basic-state heat ( $\bar{F}_\theta$ ) and moisture ( $\bar{F}_q$ ) fluxes implicit in the formulation of the equations. Analogous to the preceding derivation, the perturbation surface momentum stresses can be defined as

$$\tau'_{xz} = C_D \left\{ |\mathbf{v}| u' + (|\mathbf{v}| - |\bar{\mathbf{V}}|) \bar{U} \right\}_{z_0}, \quad (8a)$$

$$\tau'_{yz} = C_D \left\{ |\mathbf{v}| v' + (|\mathbf{v}| - |\bar{\mathbf{V}}|) \bar{V} \right\}_{z_0}, \quad (8b)$$

where  $C_D$  is the drag coefficient. Over water,  $C_D = C_E$ , and over land,  $C_D = 3 \times 10^{-3}$ .

### 2.3 | Subgrid-scale turbulence closure

We base our subgrid-scale turbulence parametrization on the first-order turbulence closure discussed in Rotunno and Emanuel (1987) and Skamarock *et al.* (2008), with special considerations for our inclusion of a basic state. For compactness, we use tensor notation, with the wind components defined as  $\mathbf{u} = \langle u_1, u_2, u_3 \rangle$  and the coordinate system as  $\mathbf{r} = \langle x_1, x_2, x_3 \rangle$ . The tendencies of the perturbation wind due to subgrid-scale turbulence can be represented as

$$T'_{u_i} = \frac{\partial \tau'_{ij}}{\partial x_j}. \quad (9)$$

The stress tensor  $\tau'_{ij}$  is defined as

$$\tau'_{ij} = K(\mathbf{r}, t) d'_{ij}, \quad (10)$$

where  $K$  is a mixing coefficient and  $d'_{ij}$  is the rate of deformation tensor, defined as

$$d'_{ij} = \frac{\partial u'_i}{\partial x_j} + \frac{\partial u'_j}{\partial x_i}. \quad (11)$$

The tendencies for a generic perturbation scalar quantity  $a$  due to subgrid-scale turbulence can be represented as

$$T'_a = -\frac{\partial F'_j{}^a}{\partial x_j}, \quad (12)$$

where  $F'_j{}^a = -K(\mathbf{r}, t) \partial a' / \partial x_j$ .

We parametrize the mixing coefficient  $K$  using

$$K(\mathbf{r}, t) = C_s^2 l_{h,v}^2 (D^2 - P_r^{-1} N^2)^{1/2}, \quad (13)$$

where  $C_s = 0.25$ ,  $P_r^{-1} = 3$ ,  $N^2$  is the Brunt–Väisälä frequency, and  $D^2$  is a function of the deformation of the flow. If the quantity  $D^2 - P_r^{-1} N^2$  is less than zero,  $K$  is set to zero. As in Skamarock *et al.* (2008), we set the vertical mixing length  $l_v$  equal to the vertical grid spacing, which is a function of height. The horizontal mixing length  $l_h$  is set to 2,000 m. This value is less than that of Skamarock *et al.* (2008), who suggests using a value equal to the horizontal grid spacing (i.e., 6,000 m) for anisotropic turbulence, but is closer to the 3,000 m used in Rotunno and Emanuel (1987). Upon testing, we found that the higher values used by Skamarock *et al.* (2008) and Rotunno and Emanuel (1987) appeared to be overly diffusive and thus we opted for a smaller value. We also noted that the decreasing amount of energy dissipation accompanying decreases in  $l_h$  tend to be compensated by increases in energy dissipated through numerical diffusion, thus decreasing overall sensitivity to changes in  $l_h$ .

The total rate of deformation is defined as

$$D_{ij} = d'_{ij} + \frac{\partial \bar{U}_i}{\partial x_j} + \frac{\partial \bar{U}_j}{\partial x_i}, \quad (14)$$

and  $D^2$  is defined as

$$D^2 = \frac{1}{2} [D_{11}^2 + D_{22}^2 + D_{33}^2] + D_{12}^2 + D_{13}^2 + D_{23}^2. \quad (15)$$

The Brunt–Väisälä frequency is defined as

$$N^2 = g \left[ A \frac{\partial \theta_e}{\partial z} - \frac{\partial (q + c + r)}{\partial z} \right], \text{ if saturated,} \quad (16a)$$

$$N^2 = g \left[ \frac{1}{\theta} \frac{\partial \theta}{\partial z} + 0.61 \frac{\partial q}{\partial z} - \frac{\partial c}{\partial z} - \frac{\partial r}{\partial z} \right], \text{ if unsaturated,} \quad (16b)$$

and

$$A \equiv \frac{1}{\theta} \frac{1 + \frac{Lq}{R_d T}}{1 + \frac{0.622 L^2 q}{c_p R_d T^2}}, \quad (17)$$

where  $\theta_e$  is equivalent potential temperature,  $L$  is the latent heat of vaporization,  $R_d$  the dry gas constant, and  $c_p$  the

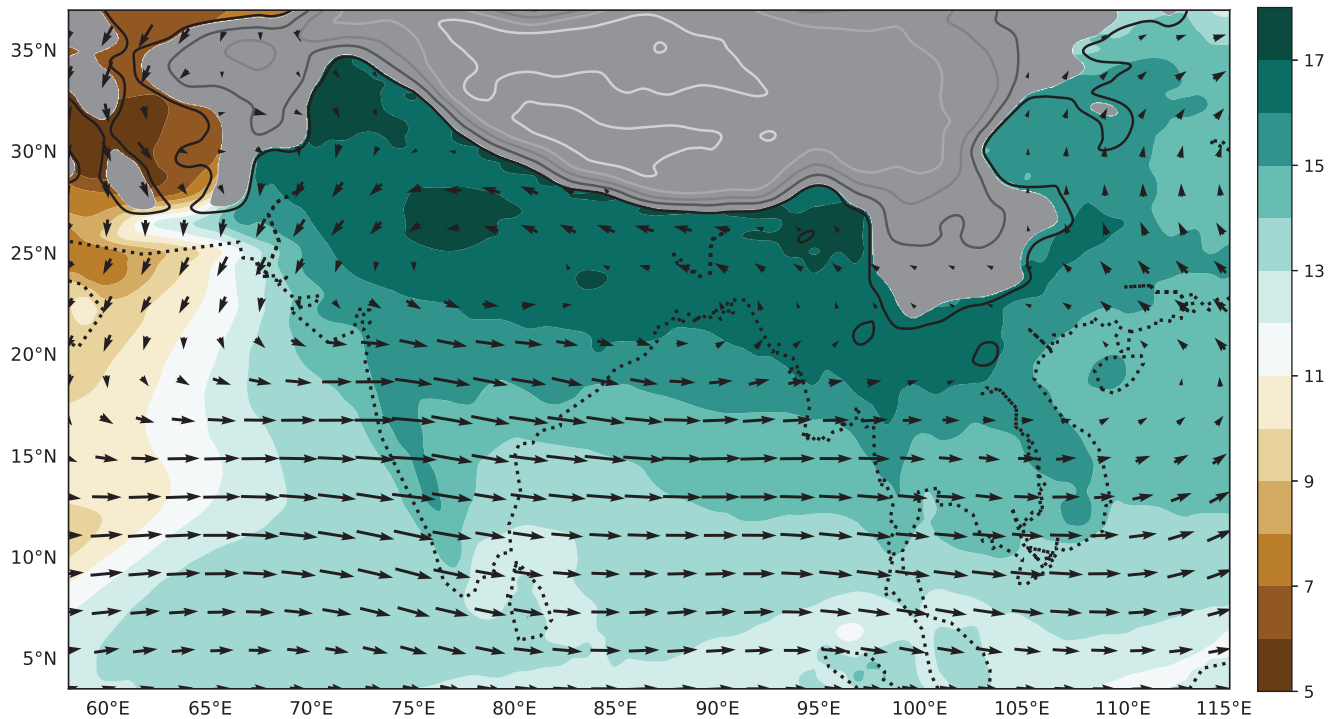


**FIGURE 1** Basic-state water-vapor mixing ratio at 1.16 km (shading,  $\bar{q} + q_0$ , g/kg), basic-state wind at 3.36 km (vectors,  $\bar{V}$ ), and terrain height (contoured every 1.0 km starting at 1.0 km). Areas below the terrain surface are shaded in gray and wind vectors with magnitudes less than 2 m/s are excluded

specific heat of air at constant pressure. All values pertaining to atmospheric fields in Equations 16 and 17 are calculated from the full fields, that is, basic state plus perturbation.

## 2.4 | Basic state, initialization, and model grid parameters

The basic state (i.e.,  $\bar{U}$ ,  $\bar{V}$ ,  $\bar{W}$ ,  $\bar{\theta}$ , and  $\bar{q}$ ) used in this study is identical to that of Diaz and Boos (2019), who performed an extensive analysis of its instability characteristics for a dry atmosphere. It is obtained from a composite of atmospheric states preceding monsoon depression genesis derived from the ERA-Interim reanalysis (Dee *et al.*, 2011). As noted previously, a key feature of this basic state is that its slowest-decaying normal mode has a structure similar to that of observed monsoon depressions. Figure 1 shows the basic-state wind at 3.36 km and moisture field at 1.16 km of the full model domain. An important feature of the background environment for monsoon depressions is the west-to-east elongated monsoon trough, along the axis of which the zonal wind shifts direction. Monsoon depressions generally form within this trough and track westward along its axis. Low-level moisture is abundant within the monsoon trough, with slowly decreasing values to the south and rapidly decreasing values to the west of India in the desert regions. Although this basic state was chosen to be representative of that in which monsoon depressions typically form, the large-scale weather pattern in this region

can vary considerably from day to day. Thus, an important caveat to keep in mind throughout this study is that different growth mechanisms could be operating for monsoon depressions that form in basic states substantially different from the one explored here.

Choosing a suitable perturbation field (i.e.,  $u'$ ,  $\theta'$ , and  $q'$ ) to initialize the simulation is complicated by lack of knowledge of the initial disturbances from which monsoon depressions typically arise. For lack of a better option, we use the least stable normal mode of this basic state obtained in the dry simulation of Diaz and Boos (2019). This method has some precedent, with a number of previous idealized instability analyses using the most unstable linear normal mode to initialize nonlinear dry and moist experiments (Thorncroft and Hoskins, 1994; Lambaerts *et al.*, 2011; 2012). This choice also has the benefit of making our results more comparable with those of Diaz and Boos (2019). Since the dry normal mode has no perturbation moisture field, the initial  $q'$  is set to zero.

All of our experiments use 6 km grid spacing. Although this resolution is coarser than typically recommended for convection-resolving simulations (e.g., Weisman *et al.*, 1997), we found little difference between a 6- and a 4-km simulation and decided that using finer resolution was not worth the additional computing resources. Interestingly, we were able to get reasonable simulations up to about 25 km grid spacing, perhaps because synoptic-scale dynamics organize the moist convection on larger scales. For monsoon depressions

themselves, this outcome is consistent with the results of Hunt and Turner (2017a), who found only marginal improvements in the structure of monsoon depressions simulated in the Met Office Unified Model as the resolution was refined beyond about a 39-km grid spacing. However, since their simulation included a convective parametrization, it may not be directly comparable. Nevertheless, our results do not seem to be overly sensitive to resolution, at least within the above-stated ranges. With 6 km grid spacing, our domain, which stretches from 58.0°E to 115°E and 3.5°N to 36°N, requires 1,060 by 620 grid points. The domain extends to 20 km in the vertical and consists of 42 vertical levels. The vertical grid spacing is stretched from 50 m at the lowest level to 1,000 m at the uppermost level using the technique of Anthes (1970).

### 3 | RESULTS

Most of our analysis will be dedicated to a control simulation that we deem to represent best the development of a monsoon depression in the Bay of Bengal. We then analyze a series of sensitivity experiments designed to elucidate some of the physical processes important for the growth of the simulated disturbance.

#### 3.1 | Disturbance structure and energetics

Figure 2 shows the time evolution of the perturbation pressure ( $p'$ ) and wind ( $\mathbf{v}'$ ) overlaid with the basic state zonal wind ( $\bar{U}$ ) at 3.36 km above sea level. At Day 2 of the simulation, a weak area of low pressure is approaching the Bay of Bengal with an area of higher pressure to its west. This low pressure amplifies as it moves over the ocean (Day 4) and makes landfall over northeastern India (Day 6). As it moves over land, it weakens and a region of high pressure forms to its east (Days 8 and 10). By Day 12, the entire wave train is weakening as it continues moving westward. The evolution of this disturbance is similar to that of observed monsoon depressions, though its lifespan lies at the higher end of typical values (Krishnan *et al.*, 2011). A possible explanation for this longer lifespan is that the basic state, which was chosen to favor monsoon depression formation, does not change with time.

Figure 3 shows a cross-section of the perturbation wind and potential temperature ( $\theta'$ ) through the center of the low pressure at 6.3 days into the simulation, a time shortly after landfall. The section is drawn to be roughly parallel to the axis of the monsoon trough, such that it passes directly through the wind maxima on either side of the low pressure center. The wind values shown are the components orthogonal to the plane of the cross-section. To highlight the larger-scale structure of the disturbance, both fields are averaged 240 km on either side of the cross-section. Similar to observed monsoon depressions (e.g., Hurley and Boos, 2015; Hunt *et al.*, 2016), this disturbance has a warm-over-cold core structure with a

lower-to-middle tropospheric maximum in perturbation wind. Although the warm core is centered near 9 km at this time, the altitude of this center varies throughout the evolution of the vortex, from near 5 km during its early phase to near 10 km at later times.

To understand better the physical processes that lead to the growth of this disturbance, we examine the time evolution of its perturbation kinetic energy, defined as  $K_p \equiv 0.5(u'^2 + v'^2)$ . For the model equation set, the rate of change of  $K_p$  can be expressed as

$$\begin{aligned} \frac{\partial K_p}{\partial t} &+ (\bar{\mathbf{U}} + \mathbf{u}') \cdot \nabla K_p + u'v'\partial_y\bar{U} + u'v'\partial_x\bar{V} + u'^2\partial_x\bar{U} \\ &+ v'^2\partial_y\bar{V} + u'w'\partial_z\bar{U} + v'w'\partial_z\bar{V} \\ &= -\mathbf{v}' \cdot \left( \frac{\partial\phi'}{\partial x}\hat{\mathbf{i}} + \frac{\partial\phi'}{\partial y}\hat{\mathbf{j}} \right) + \mathbf{v}' \cdot (T_u'\hat{\mathbf{i}} + T_v'\hat{\mathbf{j}}) \\ &+ \mathbf{v}' \cdot (n_u'\hat{\mathbf{i}} + n_v'\hat{\mathbf{j}}). \end{aligned} \quad (18)$$

On the left-hand side, the first term represents the local change of  $K_p$ , the second term represents advection of  $K_p$ , and the remaining terms represent barotropic conversion. On the right-hand side, the first term represents work done by the pressure gradient force, the second term represents tendencies from friction and subgrid-scale turbulence, and the final term is the diffusion implicit in the numerical method used to calculate advection, with  $\mathbf{n}'$  being the velocity tendency vector due to this process. For succinctness, we combine the barotropic terms into a horizontal shear term ( $u'v'\partial_y\bar{U} + u'v'\partial_x\bar{V}$ ), a horizontal convergence term ( $u'^2\partial_x\bar{U} + v'^2\partial_y\bar{V}$ ), and a vertical shear term ( $u'w'\partial_z\bar{U} + v'w'\partial_z\bar{V}$ ). Figure 4 shows the time evolution of each term averaged over the entire model domain, with Figure 4a,b showing them expressed as the rate of energy generation and Figure 4c,d as growth rates. To highlight the correspondence between precipitation and pressure work, Figure 4a also shows the rain-water mixing ratio averaged within a  $15^\circ \times 15^\circ$  box centered on the minimum pressure.

During most of the first two days,  $K_p$  is decaying. The dominant energy source is from horizontal shear, with the other terms remaining small or negative. Growth rates increase rapidly beyond day 2, as the pressure work term becomes dominant. This sudden increase in pressure work coincides with the increase in rain water (Figure 4a). Thus, we attribute this energy to latent heat release from convection decreasing hydrostatic pressure, which in turn leads to an acceleration of the perturbation wind. From day 4–8, growth waxes and wanes, with positive contributions mainly from pressure work and horizontal shear and losses from friction and numerical diffusion. The growth rates of about  $0.25\text{--}0.3\text{ d}^{-1}$  from horizontal shear throughout the simulation are similar to that of the most unstable normal mode of this basic state (figure 11 in Diaz and Boos (2019)). By day 9, the total growth rate becomes permanently negative as the

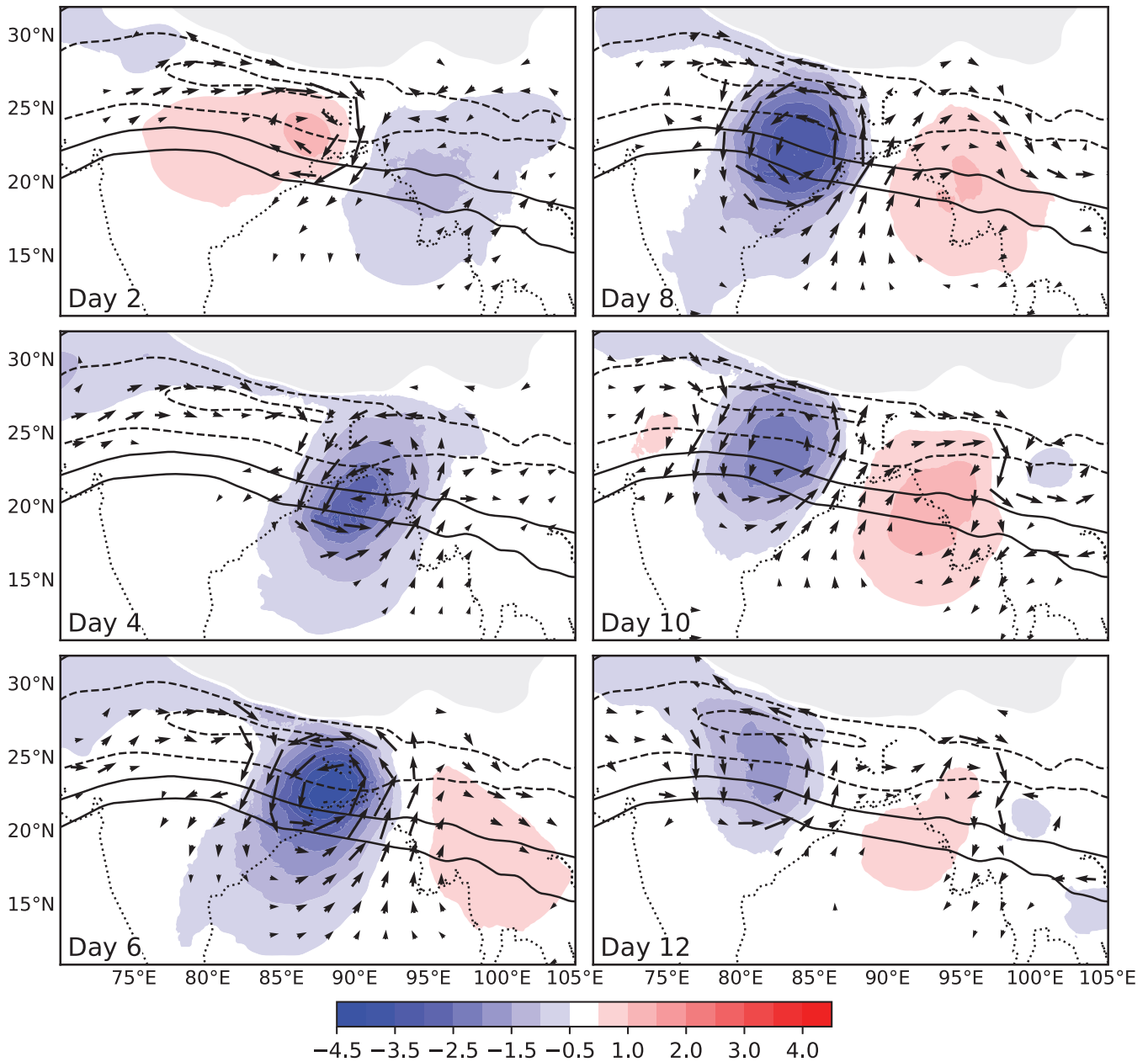


**FIGURE 2** For the control simulation, time evolution of perturbation pressure at 3.36 km ( $p'$ , shading, hPa), perturbation winds at 3.36 km ( $\mathbf{v}'$ , vectors), and basic-state zonal wind at 3.36 km ( $\bar{U}$ , contoured every 4 m/s between  $-6$  and  $6$  m/s). Areas below the terrain are shaded in gray and wind vectors less than  $2$  m/s are excluded

disturbance decays. The gradual loss of pressure work as a dominant energy source corresponds with a decrease in precipitation. However, meridional shear continues to be a large energy source, slowing down its overall decay as it moves inland.

In comparison with the results of Diaz and Boos (2019), the disturbance in this simulation exhibits many of the features of the least stable dry normal mode of this basic state, including its overall size, track, vertical structure, and the fact that it gains energy from the meridional shear of the basic state. A major difference is that, with the addition of moist convection, this disturbance amplifies, with a

large source of energy coming from pressure work. The following section will detail how this convection leads to its amplification.

### 3.2 | Role of convection in vortex amplification

The interaction with latent heat release is essential for the disturbance presented in section 3.1 to achieve net growth. This necessity will be demonstrated explicitly in section 3.3. Here, we explore how the disturbance organizes convection and how this convection leads to its amplification.

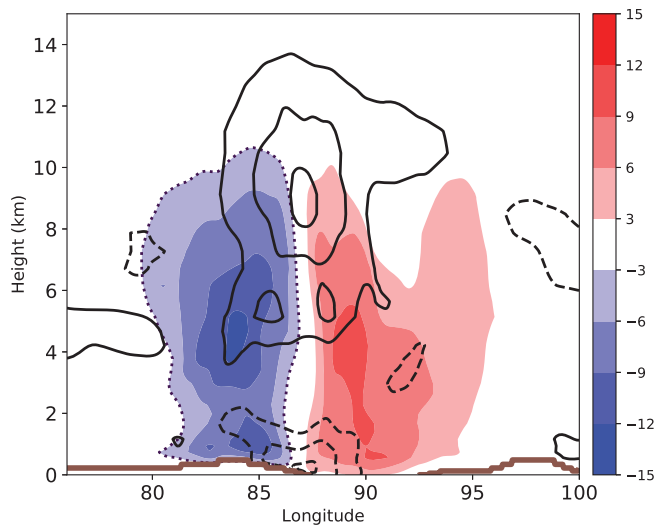


**FIGURE 3** Cross-section from  $[26.5^{\circ}\text{N}, 75^{\circ}\text{E}]$  to  $[18^{\circ}\text{N}, 100^{\circ}\text{E}]$  at 6.3 days. Fields shown are perturbation wind components orthogonal to the plane of the cross-section (shading, m/s) and perturbation potential temperature (contoured every  $0.8\text{ K}$ ,  $\theta'$ ). The thicker line demarcates the terrain surface and negative values of wind are enclosed within the dotted line [Colour figure can be viewed at [wileyonlinelibrary.com](http://wileyonlinelibrary.com)].

### 3.2.1 | Organization of the rain field

One distinguishing feature of monsoon depressions is their asymmetric precipitation field. Whereas precipitation in well-organized tropical cyclones is roughly symmetric about their center, precipitation in monsoon depressions is biased toward the southwestern quadrant of their circulation (Godbole, 1977; Sanders, 1984). To summarize the precipitation field in our simulation, we examine a mass-weighted average of rain-water mixing ratio ( $r$ ) from 0.4–15.0 km (Figure 5). For reference, this quantity is overlaid with the perturbation pressure ( $p'$ ) and wind field ( $\mathbf{v}'$ ), both at 3.36 km and smoothed with a Gaussian filter to emphasize the larger-scale circulation. Figure 5a shows these fields at 3.7 days (88 hr) into the simulation, a time roughly coinciding with the peak growth rate (Figure 4). At this time, rain is most extensive and intense south and west of the circulation center, with the highest values located about 300 km west of center. Rain in the vicinity of the center is much weaker and more scattered. As noted above, this pattern is typical of monsoon depressions. By 4.8 days (114 hr), a time near the peak vortex intensity, the heaviest rain has become concentrated into a band located south and west of the circulation center, with the central region becoming devoid of precipitation (Figure 5b). By 7.6 days (182 hr), the rain has become less intense but is still widespread (Figure 5c). This decreasing precipitation aligns well with the decreasing growth rates from pressure work (Figure 4).

The precipitation distribution within monsoon depressions has generally been linked to their interaction with the

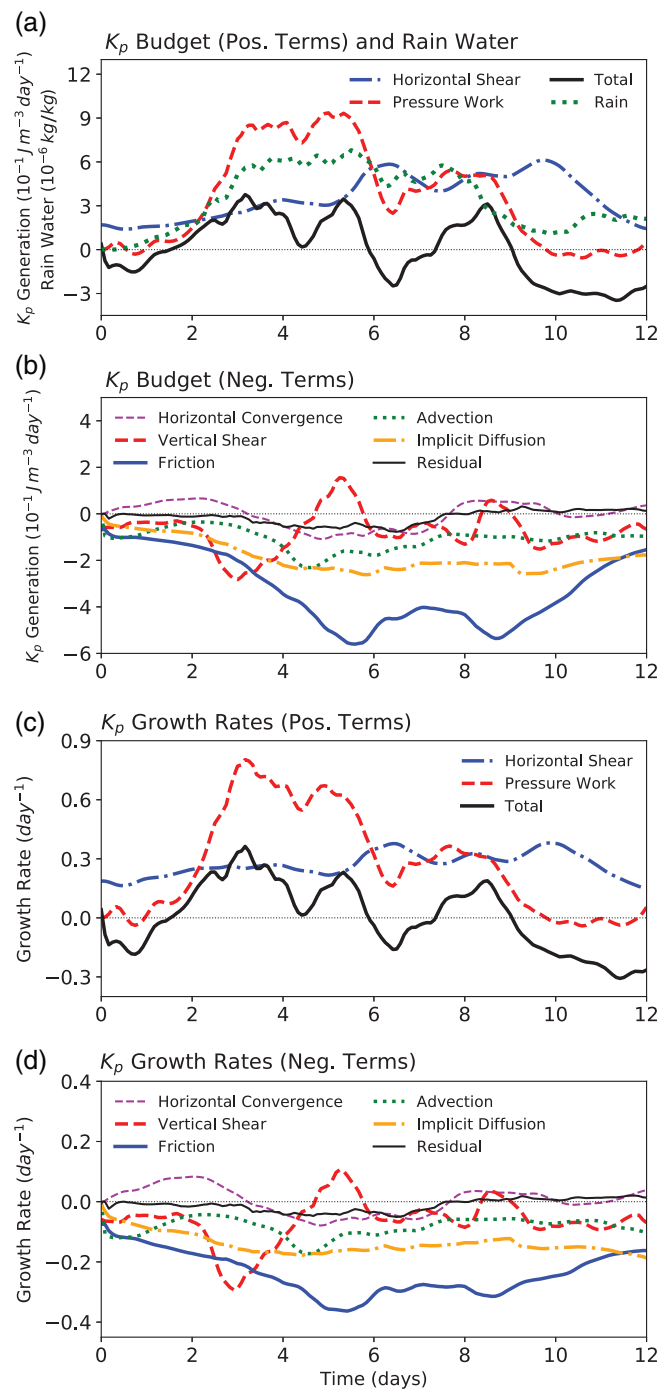


**FIGURE 4** Domain-averaged terms in the  $K_p$  budget (Equation 18). Panel (a) shows  $K_p$  generation rates for the predominately positive terms, along with the rain-water mixing ratio averaged within a  $15^{\circ} \times 15^{\circ}$  box centered on the minimum pressure, (b) shows the generation rates for the predominately negative terms, (c) shows the corresponding growth rates for the terms shown in (a), and (d) similarly for the terms shown in (b). For all plots, a 6-hr moving average is applied to smooth out the higher frequency noise [Colour figure can be viewed at [wileyonlinelibrary.com](http://wileyonlinelibrary.com)].

background wind shear and temperature gradient associated with the large-scale monsoon (e.g., Rao and Rajamani, 1970; Rajamani and Rao, 1981; Sanders, 1984; Boos *et al.*, 2015;

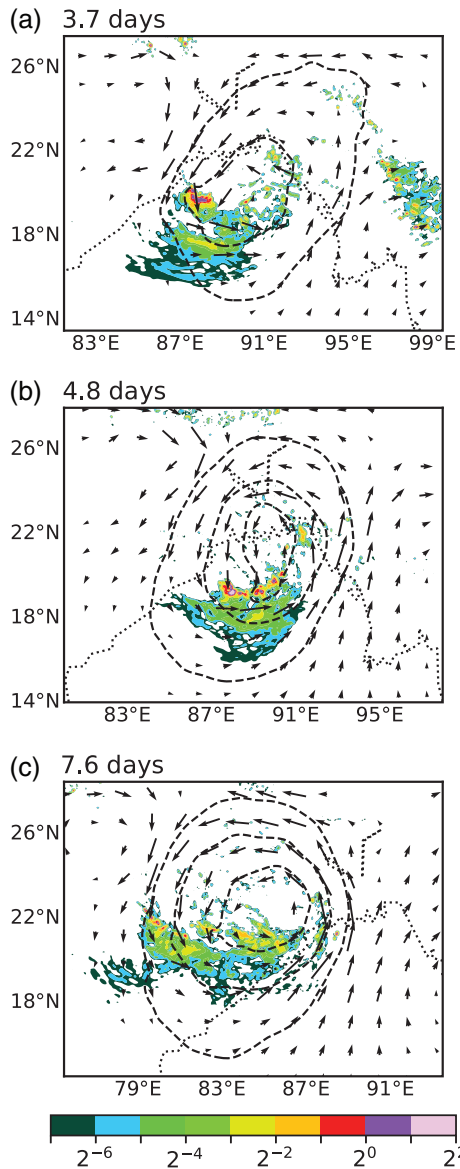


**FIGURE 5** Time evolution of rain-water mixing ratio ( $r$ , shading, g/kg, 0.08–15 km mass-weighted average), perturbation pressure ( $p'$ , contours, 3.36 km), and perturbation winds ( $\mathbf{v}'$ , vectors, 3.36 km) for the control simulation at (a) 3.7 days (88 hr), (b) 4.8 days (114 hr), and (c) 7.6 days (182 hr). To emphasize the broader-scale pattern, the pressure field has been smoothed with a Gaussian filter

Adames and Ming, 2018b). This interaction has been most frequently expressed using the quasigeostrophic (QG) omega equation. Following this approach, we use the  $\mathbf{Q}$ -vector form of the QG-omega equation. Starting with the height coordinate version (Hoskins *et al.*, 1978; Hoskins, 1997) and retaining the separation between the basic state and perturbation, the two components of the  $\mathbf{Q}$ -vector become

$$Q_1 = -\frac{g}{\theta_0} \left( \frac{\partial \bar{\mathbf{V}}}{\partial x} \cdot \nabla_h \theta' + \frac{\partial \mathbf{v}'_{\psi}}{\partial x} \cdot \nabla_h \bar{\theta} + \frac{\partial \mathbf{v}'_{\psi}}{\partial x} \cdot \nabla_h \theta' \right), \quad (19a)$$

$$Q_2 = -\frac{g}{\theta_0} \left( \frac{\partial \bar{\mathbf{V}}}{\partial y} \cdot \nabla_h \theta' + \frac{\partial \mathbf{v}'_{\psi}}{\partial y} \cdot \nabla_h \bar{\theta} + \frac{\partial \mathbf{v}'_{\psi}}{\partial y} \cdot \nabla_h \theta' \right). \quad (19b)$$

Following previous applications of the QG-omega equation in the Tropics (Kiladis *et al.*, 2006; Boos *et al.*, 2015), we have substituted the rotational component of the wind ( $\mathbf{v}'_{\psi}$ ) for the geostrophic wind. For simplicity, we have used the full basic-state wind instead of its rotational component. The QG-omega equation can be expressed as

$$\left( N^2 \nabla_h^2 + f_o^2 \frac{\partial^2}{\partial z^2} \right) w'_q = 2 \nabla_h \cdot \mathbf{Q} + \beta \frac{g}{\theta_0} \frac{\partial \theta'}{\partial x}, \quad (20)$$

where  $\beta$  is the meridional gradient of the Coriolis parameter and  $w'_q$  is the perturbation QG vertical velocity. The quantity  $w'_q$  can then be determined by inverting the operator on the left-hand side of Equation 20. At all boundaries, we assume that  $w'_q$  goes to zero. This matches the boundary condition for  $w'$  in the model equation set. The resulting  $w'_q$  field corresponding to times in Figure 5 is shown in Figure 6, along with the 3.36-km perturbation stream function ( $\psi'$ ). To provide a more integrated perspective of QG vertical motion, the  $w'_q$  field is averaged from 1.45 to 5.36 km above sea level. Because of the simulation's high resolution, considerable spatial variability occurs in the vicinity of the convection. Since QG dynamics are presumably less applicable at this fine scale, the following discussion focuses on the broader-scale  $w'_q$  structure.

At 3.7 days, QG ascent lies south and west of the circulation center, with QG descent to the northeast (Figure 6a). This arrangement corresponds well with the precipitation field, which has extensive rain to the southwest and little rain to the northeast (Figure 5a). Observed monsoon depressions exhibit a similar dipole of QG vertical motion (e.g., figure 4 in Boos *et al.* (2015)). The positive  $w'_q$  values of 1–2 cm/s west of the circulation center are of similar magnitude to the actual vertical velocity ( $w'$ ) of the dry simulations of figure 15 of Diaz and Boos (2019). The pattern of QG ascent remains similar at 4.8 days, with ascent to the south and west and descent to the north and east (Figure 6b). At this time, precipitation occurs within the southern portion of the QG ascent region (Figure 5b). This offset could result from the delay between when an air parcel begins its ascent and when it becomes saturated with water vapor, during which time it is advected southward. The pattern of QG ascent changes by 7.6 days, with a large area of QG ascent west of the circulation center and a small area of QG descent to the east (Figure 6c). Though precipitation remains within areas of positive  $w'_q$  (Figure 5c), a large region of QG ascent unaccompanied by precipitation occurs north of the vortex. Again, we speculate that this offset may be attributed to a delay between the start of ascent and the onset of saturation.

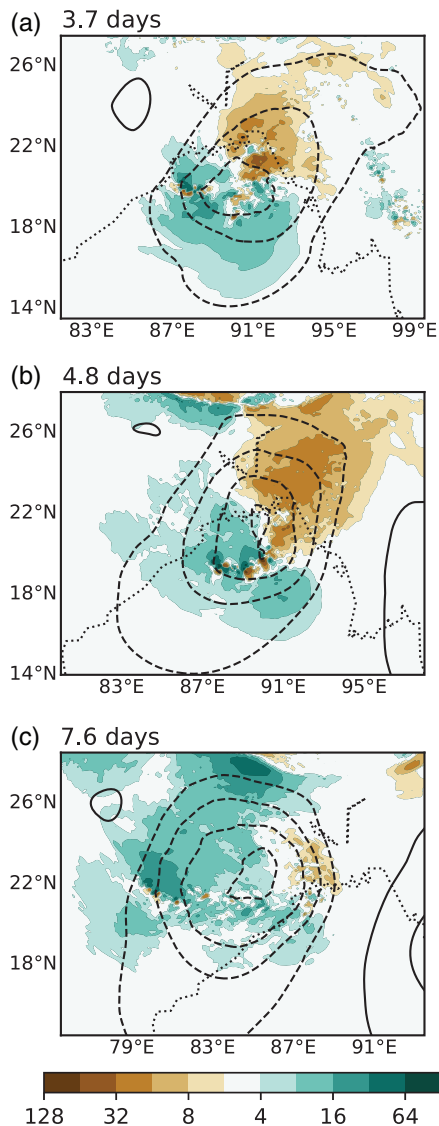


**FIGURE 6** Time evolution of vertical velocity ( $w'_q$ ) from the QG-omega equation (Equation 20) (shading, mm/s, 0.04–5.13 km average) and perturbation stream function ( $\psi'$ ) at 3.36 km (contours) for the control simulation at (a) 3.7 days, (b) 4.8 days, and (c) 7.6 days

### 3.2.2 | Potential vorticity analysis

We now work toward understanding how latent heat release amplifies the circulation. Previous studies showed that the dominant source of rotation in monsoon depressions comes from vorticity stretching, presumably from the vertical motion coupled to convection (Daggupati and Sikka, 1977; Boos *et al.*, 2015). To make this link more explicit, we use a potential vorticity budget, in which the contribution from latent heating can be isolated. Recognizing the partition between perturbation and basic state, the perturbation potential vorticity ( $P'$ ) is expressed as

$$P' = \frac{1}{\rho_0} [\zeta' \cdot \nabla(\bar{\theta} + \theta_0) + (\bar{\zeta}_a + \zeta') \cdot \nabla\theta'], \quad (21)$$

where  $\zeta$  and  $\zeta_a$  are the relative and absolute vorticity vectors, respectively, and the prime and bar notation follows the same logic as the original governing equation set. The distribution of  $P'$  generated from diabatic heating over the time interval  $T_1$  to  $T_2$  can be expressed as

$$P'_d = \frac{1}{\rho_0} \int_{T_1}^{T_2} (\bar{\zeta}_a + \zeta') \cdot \nabla M'_\theta dt. \quad (22)$$

The potential vorticity framework is useful because, through the invertibility principle (Hoskins *et al.*, 1985), one can conceive of the  $P'$  generated by latent heat release as contributing to the larger-scale circulation of the monsoon depression. Additionally, since  $P'$  is conserved following the flow in the absence of  $P'$  sources and sinks, one can envision  $P'$  being generated by convection and then passively advected to regions away from the convection, as will be elaborated upon in section 3.2.3. The time evolution of  $P'$  and  $P'_d$  averaged from 0.4–5.13 km is shown in Figure 7, with perturbation winds ( $\mathbf{v}'$ ) at 3.36 km overlaid. Values of  $P'_d$  in each plot are integrated over the 2 hr previous to the time shown and then converted to an hourly generation rate. To make the fields more presentable, they are smoothed with a Gaussian filter and plotted on a  $\log_2$  scale for  $P'$  and a  $\log_3$  scale for  $P'_d$ .

At 3.7 days, a broad region of higher  $P'$  is located within the circulation center (Figure 7a). However, the largest  $P'$  and  $P'_d$  are positioned well to the west of the circulation center in the region of maximum precipitation (Figure 5a). Values of  $P'_d$  near the circulation center, though nonzero, are about one to two orders of magnitude smaller than those far to the west. This arrangement of  $P'$  and  $P'_d$  resembles the vorticity budgets examined in previous studies, where the maximum vorticity production through vorticity stretching occurs southwest of the vortex center in the region of highest precipitation (Daggupati and Sikka, 1977; Krishnan *et al.*, 2011; Boos *et al.*, 2015). By 4.8 days, the maximum  $P'_d$  has become concentrated within the precipitation band on the southern side of the vortex (Figure 7b). A broad area of high  $P'$  remains located within the vortex center, though it is separated from the region of  $P'_d$ . By 7.6 days, the central region of  $P'$  has become fragmented with an east-to-west oriented region of  $P'_d$  (Figure 7c). This transformation is consistent with the weakening rain field (Figure 5c) and a decreasing amount of energy generated from pressure work (Figure 4).

### 3.2.3 | Trajectory analysis

As seen in section 3.2.2, the region of highest  $P'_d$  associated with convection is offset south and west of the circulation center. However, large values of  $P'$  have also accumulated within the circulation center, away from the convection. A reasonable explanation is that this  $P'$  was created within the precipitating region and then passively advected downstream.

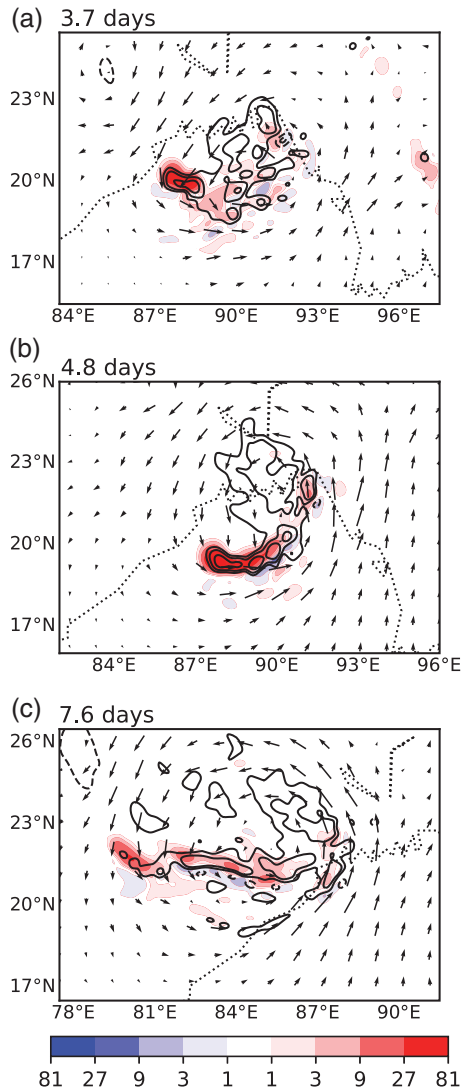


**FIGURE 7** Time evolution of diabatic generation of perturbation PV ( $P'_d$ , shading, 0.7 PVU/hr, 0.08–15 km mass-weighted average), perturbation winds at 3.36 km ( $v'$ , vectors), and perturbation PV ( $P'$ , contoured on a  $\log_2$  scale beginning at 0.3 PVU) for the control simulation at (a) 3.7 days, (b) 4.8 hr, and (c) 7.6 days. Values of  $P'_d$  in each plot are integrated over the 2 hr previous to the time shown and then converted to an hourly generation rate. To emphasize the broader-scale pattern, the PV and PV generation field have been smoothed with a Gaussian filter

This process can readily be seen in animations of potential vorticity (not shown). Here, we test this supposition by calculating trajectories forward in time emanating from the region of maximum  $P'_d$ . We focus on the interval from 80–116 hr, near the period of peak growth (Figure 4). Results are shown in Figure 8. The dashed-line box, which is drawn to enclose roughly the region of strongest convection (shading) and thus highest  $P'_d$ , delineates the region from which the trajectories are specified to originate. The vertical profile of  $P'$  and  $P'_d$  averaged over this box is shown in Figure 9. With  $P'$  generation at low levels and  $P'$  destruction at high levels, this profile is more characteristic of convective heating

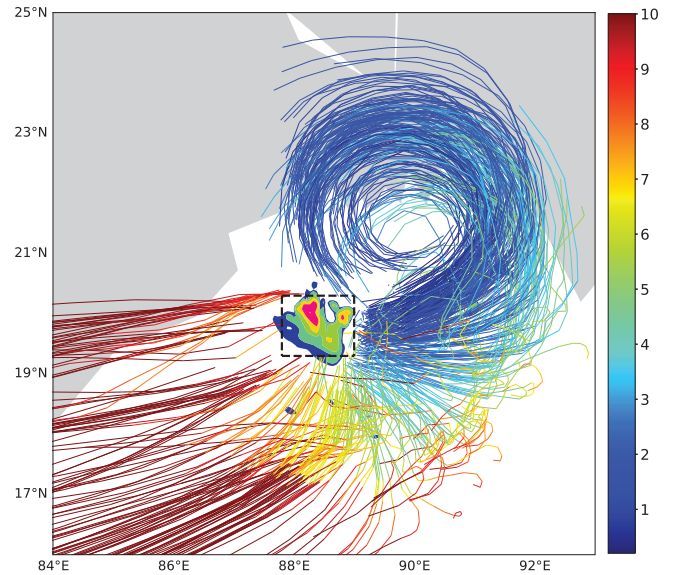


**FIGURE 8** Trajectory paths colored by altitude (km) from 80–116 hr. The dashed-line box shows the starting points of the trajectories and the shading shows rain-water mixing ratio at 80 hr. The color bar corresponds to the trajectory heights

than stratiform. We note that profiles farther south are more characteristic of stratiform heating, with  $P'$  generation at upper levels and  $P'$  destruction at lower levels (not shown), consistent with Krishnan *et al.* (2011) and Boos *et al.* (2017), who noted that heating profiles in monsoon depressions tend to be more stratiform. Since  $P'_d$  within the box is largest at low levels, we limit our trajectories to those which begin between 0.41 and 2.28 km above the surface. The lines in Figure 8 depict individual trajectories colored by altitude from 80–116 hr originating from the above-described volume.

Figure 8 suggests two general paths taken by air parcels leaving the convection. Some parcels ascend high enough within the convection to be advected rapidly westward in the strong flow aloft. Others remain low enough to be advected eastward and then swept cyclonically around the circulation center. It is these eastward-moving low-level air parcels that are capable of transporting high potential vorticity generated at low levels by diabatic heating toward the circulation center, where they can accumulate and contribute to the amplification of the depression-scale circulation. The integrated effect of this process may explain the large values of  $P'$  in regions devoid of convection seen in Figure 7.

This intensification mechanism, incorporating both the potential vorticity and trajectory analysis, is summarized in Figure 10. The path of the  $P'$  center of mass from 56–116 hr is marked with  $\times$  symbols and the path of the  $P'_d$  center of mass is marked by  $+$  symbols (Figure 10a). Both are calculated

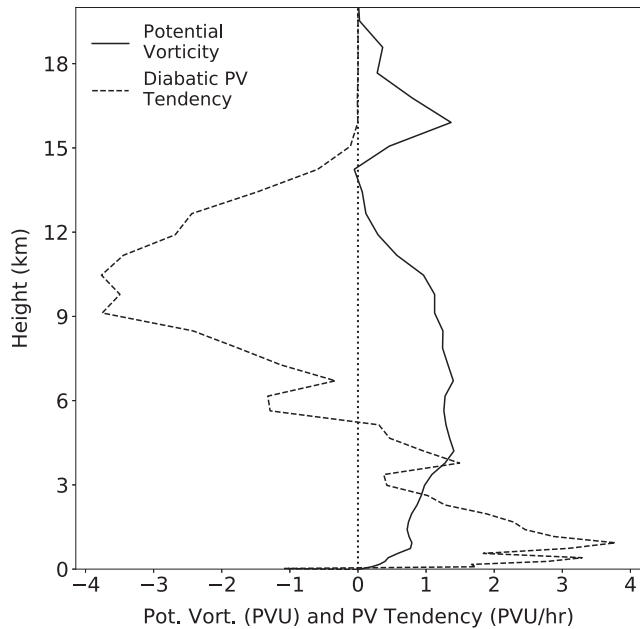


**FIGURE 9** Vertical profile of  $P'$  and  $P'_d$  averaged over the box shown in Figure 8 at 80 hr. As in Figure 7, the values of  $P'_d$  are integrated over 2 hr previous to this time and converted to an hourly rate

using positive values averaged from 0.41–5.13 km above the surface. The arrowed lines show two median trajectory paths emanating from the region of maximum  $P'_d$  over the 80–116 hr time period. The dotted line includes trajectories which, after 10 hr, lie east of the box depicted in Figure 8 and are below 2 km. The dashed line is the same, except for those lying between 2 and 5 km. The former contains 1,135 of the original 4,842 trajectories and the latter 1,577. Their median altitude as a function of time is shown in Figure 10b. Over the 80–116 hr timeframe, the  $P'_d$  center of mass lies west of the  $P'$  center of mass at earlier times, with their orientation gradually shifting to southwest-to-northeast at later times. Low-level air parcels originating from the  $P'_d$  region are located within the fast westerly flow and are thus quickly advected toward the east. In fact, within a period of only 4 hr, the median trajectory is already positioned east of the  $P'$  center of mass. The two median trajectories then orbit the  $P'$  center of mass, where their vorticity is incorporated into the broader-scale circulation.

Some studies have argued that persistent vortex stretching induced by convection to the west of a circulation center causes monsoon depressions to propagate westward (e.g., Chen *et al.*, 2005). This explanation may sound reasonable from an Eulerian perspective. However, the Lagrangian perspective presented above offers a different viewpoint. Being embedded within fast westerly flow, these high-vorticity air parcels reach the longitude of the circulation center within a mere 2–4 hr (Figure 10a). Thus, vorticity advection overwhelms the local vorticity tendency caused by vortex stretching. A similar cancellation between vorticity

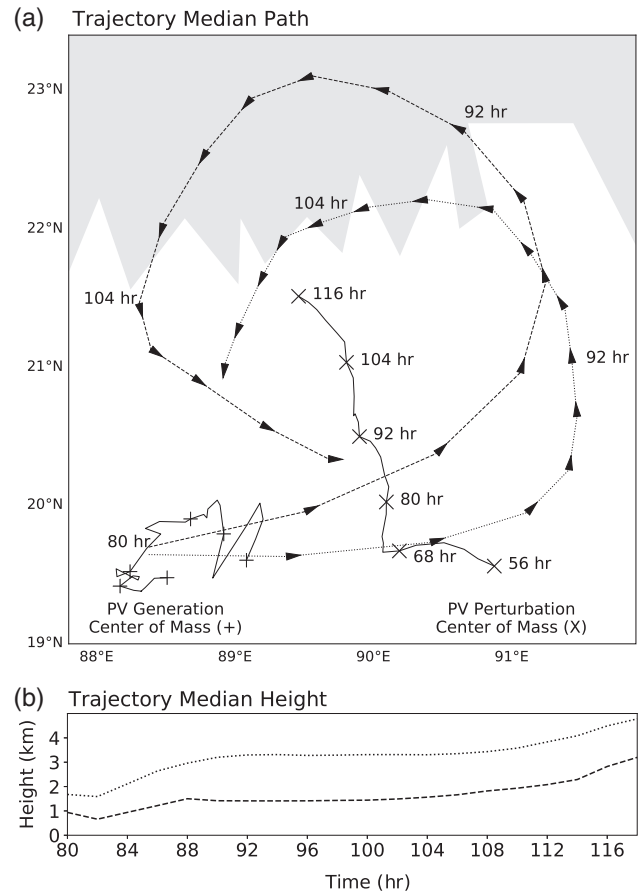


**FIGURE 10** (a) The relationship between air-parcel median trajectories (lines with directional arrows), the  $P'$  center of mass ( $\times$  symbols), and the  $P'_d$  center of mass (+ symbols). The arrows on the trajectories are drawn every 2 hr from hour 80 to hour 112 and labeled with the simulation time every 12 hr. The  $P'$  center of mass is labeled every 12 hr from hour 56 to hour 116. For the  $P'_d$  center of mass, a symbol (+) is drawn every 12 hr from hour 56 to hour 116, but for clarity this is not labeled. The easternmost symbol on its track is at hour 56. (b) The height of the two median trajectories as a function of time with line styles chosen to match those in (a)

stretching and advection for monsoon depressions was shown by Boos *et al.* (2015). This observation, along with the fact that the disturbance translates westward at a similar speed in the dry simulation (Diaz and Boos, 2019), suggests that the convection is not causing the disturbance to propagate westward.

### 3.3 | Sensitivity experiments

The previous sections focused exclusively on our control simulation, in which a rapidly growing disturbance resembling a monsoon depression drew energy from the meridional shear of the basic state and from its interaction with latent heat release. In this section, we present a series of sensitivity experiments to understand better the processes influencing this growth. These experiments will be grouped

into four categories, namely Experiments A, B, C, and D, with subexperiments under each category meant to be compared with each other and the control. For each experiment, we plot the minimum perturbation pressure 0.74 km above sea level every 2 hr, smoothed with a three-point moving average (Figure 11). To facilitate comparison, the control simulation is duplicated in each panel. However, it should be noted that there is some uncertainty in comparing individual experiments, since stochastic processes associated with convection can lead to rapid short-term fluctuations in pressure. With this in mind, our analysis focuses more on the day-to-day differences and less on the hourly ones. For each experiment, we also show the total accumulated perturbation kinetic energy associated with each term in Equation 18 (Figure 12). These values are calculated by integrating the domain-averaged energy generation rate for each term from hour 4 to hour 220 of the simulation. For an additional point of comparison, the average growth rates over this time period are shown in Figure 13.

### 3.3.1 | Energy sources (Experiment A)

Experiment A focuses on the energy sources leading to growth. As previously discussed, latent heating is essential for amplification of this disturbance. To illustrate this, we run a simulation in which we deactivate the microphysics parametrization. As expected, the disturbance fails to amplify, with the minimum perturbation pressure remaining near  $-1$  hPa (Figure 11a). Nevertheless, it still draws energy from the basic-state meridional shear (Figure 12a), with the growth rate due to this process only slightly reduced compared with the control (Figure 13a). This result is consistent with Diaz and Boos (2019), who found that this basic state can support waves that draw energy from the meridional shear, but that this energy source is insufficient to produce net growth once dissipative processes are included.

In the second part of Experiment A, we assess the role of the basic-state meridional shear by eliminating all terms in Equations 1 and 3 with overbars (i.e.,  $\bar{U}$ ,  $\bar{\theta}$ , and  $\bar{q}$ ). The result is a disturbance initialized in a horizontally homogeneous environment with basic-state temperature and moisture profiles taken from the midpoint of the domain, which lies in the northernmost Bay of Bengal. This approach is imperfect, since other features of the basic state, such as vertical and zonal gradients of wind, could also be important for the disturbance evolution. Unfortunately, the various gradients present in this basic state cannot be modified independently while maintaining realistic balance constraints. Nevertheless, this type of experiment can verify whether some aspect of the basic state is necessary for disturbance amplification. As shown in Figure 11a, without the basic state, the disturbance fails to amplify, though it does maintain a pressure near or slightly below  $-1$  hPa for the duration

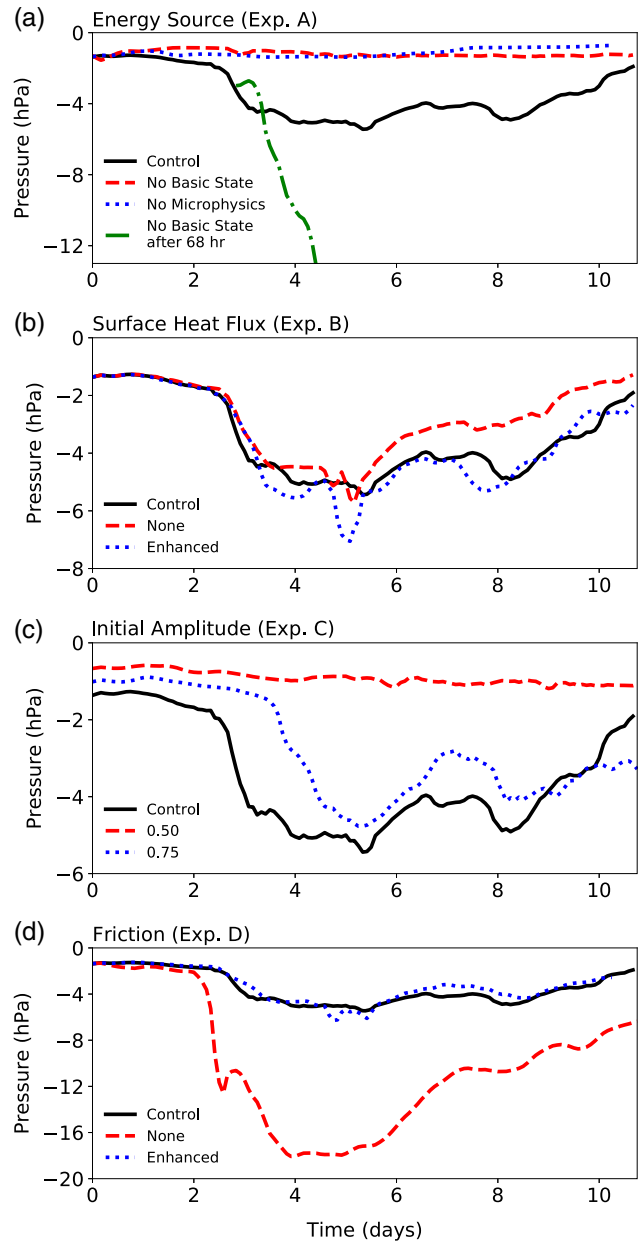


**FIGURE 11** Minimum perturbation pressure (hPa) at 0.74 km for sensitivity experiments. Results for Experiments (a) A, (b) B, (c) C, and (d) D [Colour figure can be viewed at [wileyonlinelibrary.com](http://wileyonlinelibrary.com)]

of the simulation. Isolated convection still forms within the circulation (not shown), presumably influenced by some combination of frictional convergence and surface heat fluxes, and the resulting latent heat release leads to limited growth through pressure work (Figures 12a and 13a). Though this contribution is small, the proportion of energy lost through turbulence and numerical diffusion is also much smaller relative to the control, since the disturbance does not have to contend with the basic-state shear (Figure 13a).

For the final part of Experiment A, instead of removing the basic-state gradients at the beginning of the simulation, we remove them midway through the period of rapid intensification, namely at hour 68. This scenario places

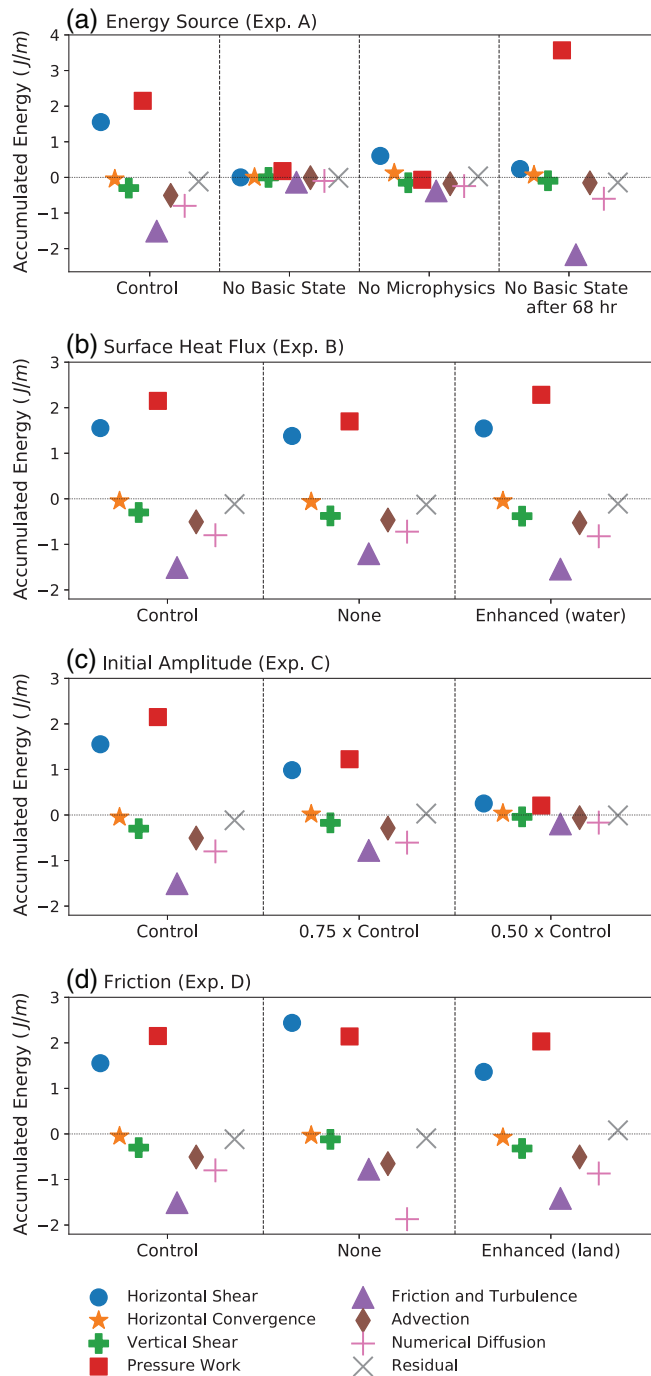


**FIGURE 12** Mass-weighted domain average accumulated kinetic energy for sensitivity experiments from hour 4 to hour 220 of each simulation. Results for Experiments (a) A, (b) B, (c) C, and (d) D [Colour figure can be viewed at [wileyonlinelibrary.com](#)]

an approximately  $-3$  hPa low-pressure area over a warm ocean with no wind shear. In this experiment, after a brief period of weakening immediately after removing the basic state, the vortex intensifies rapidly (Figure 11a). Though not shown on the plot, the perturbation pressure reaches  $-58$  hPa on day 6, after which it makes landfall and weakens. In this case, the disturbance clearly undergoes tropical cyclogenesis and intensifies through the WISHE mechanism.

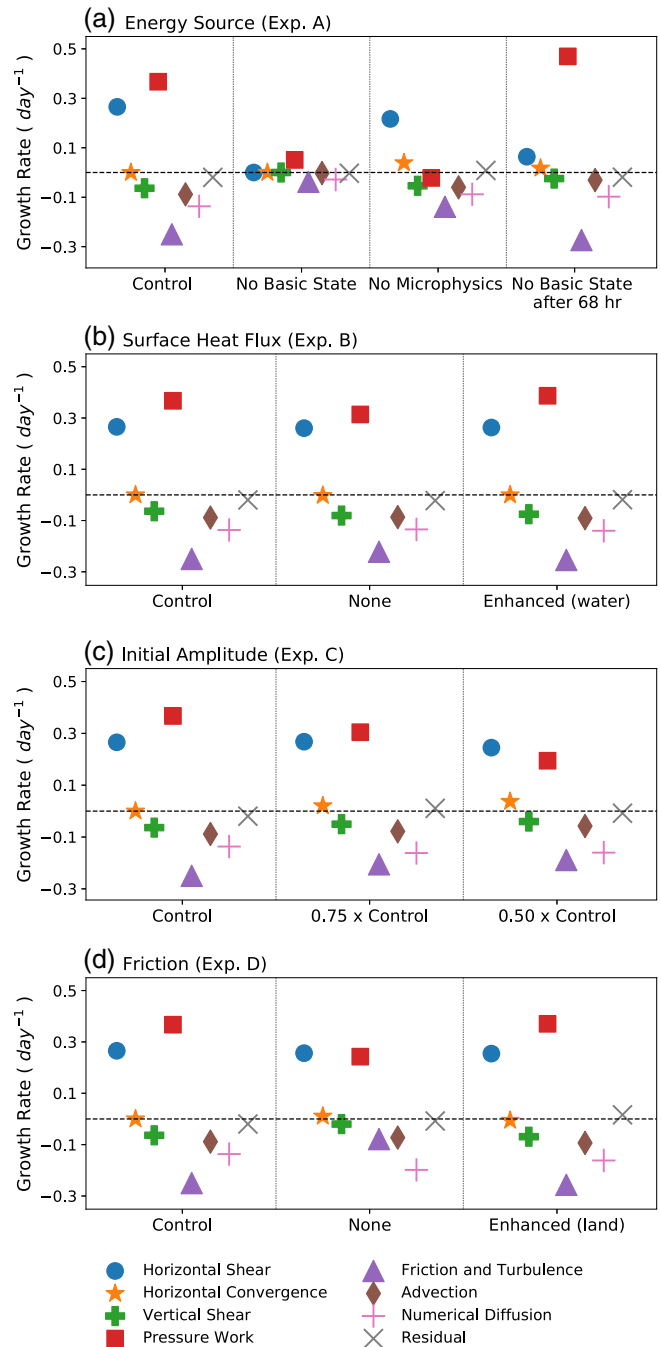


**FIGURE 13** Same as in Figure 12, but for the average growth rates [Colour figure can be viewed at [wileyonlinelibrary.com](#)]

This experiment illustrates that, though the basic state may contribute to disturbance growth initially, it is ultimately detrimental to continued amplification. This is presumably due to its strong vertical wind shear and its tendency to advect the disturbance westward into the adjacent land-mass. Interestingly, although the pressure deficit is an order of magnitude larger in this experiment relative to the control (Figure 11a), the total energy extracted is similar when both pressure work and horizontal shear are added together

(Figure 12a); the energy of the tropical cyclone is concentrated into a much smaller area compared with the monsoon depression.

### 3.3.2 | Surface heat fluxes (Experiment B)

Surface sensible and latent heat fluxes are necessary for sustained tropical cyclone amplification, and they could also be important for monsoon depressions, despite the much weaker surface winds of those storms. In Experiment B, we modify the surface flux parametrization (Equation 6) to assess the role of surface heat fluxes in the amplification of the simulated disturbance. For the first part of Experiment B, we turn off the perturbation sensible and latent heat fluxes completely by setting  $F'_q$  and  $F'_\theta$  in Equation 6 to zero. It is important to distinguish this scenario from turning off the total surface flux, as one might in a traditional modeling experiment: implicit basic-state surface fluxes  $\bar{F}_q$  and  $\bar{F}_\theta$  remain to maintain the basic-state moisture and temperature fields (Equation 4). Considering the strength of the low-level southwesterly flow in this region associated with the monsoon, the basic-state fluxes presumably contribute substantially to maintaining the basic-state moisture field. Setting  $F'_q$  and  $F'_\theta$  to zero will, however, inhibit the WISHE mechanism by preventing a feedback between surface wind and surface fluxes.

As seen in Figure 11b, a surface flux feedback plays little to no role in the initial amplification of the disturbance, since the minimum pressure is nearly the same as the control for the first five days. Afterward, however, the minimum pressure is about 1–2 hPa higher than that of the control, indicating that surface fluxes play some role in maintaining the strength of the disturbance after it has reached its maximum intensity. This is also reflected in slightly less energy gained from pressure work relative to the control (Figure 12b). Interestingly, the largest differences in intensity occur primarily after landfall (Figure 2), when one might expect surface fluxes from the ocean to be less important. The reason is that the perturbation southwesterly flow east of the circulation center remains over water and continues to contribute to the anomalous sensible and latent heat flux even after the center makes landfall. Although none of our simulations includes anomalous surface heat and moisture fluxes over land, some studies have argued that surface moisture fluxes are important for monsoon depressions to maintain their intensity over land (Hunt and Turner, 2017b).

In the second part of Experiment B, we enhance the surface sensible and latent heat fluxes by increasing the sea-surface temperature from 28.0 °C to 29.0 °C. This is accomplished by increasing the saturation mixing ratio  $q_s^*$  and surface temperature  $T_s$  in Equation 4. This results in a slightly higher intensity throughout most of the period when the disturbance is strongest (i.e., days 4–8), with negligible changes at other times (Figure 11b).

From Experiment B, we conclude that monsoon depressions do not require WISHE for their formation, but that WISHE can contribute to higher intensity, especially once a monsoon depression reaches larger amplitude.

### 3.3.3 | Initial amplitude (Experiment C)

In the next set of experiments (Experiment C), we vary the initial amplitude of the disturbance. Although theories of normal-mode baroclinic and barotropic instability allow disturbances to develop spontaneously from an infinitesimally small initial perturbation or even random noise, other theories, such as those involving growth of tropical cyclones by WISHE, require some threshold amplitude. To determine which case is more applicable here, we conduct two experiments: one with the initial amplitude reduced to 75% of its value in the control and another where it is reduced to 50%. In the former case, although the rapid amplification is delayed by about one day, it still achieves a similar, albeit slightly higher, minimum pressure (Figure 11c). However, for the latter case, the disturbance does not strengthen at all. We speculate that, when the initial amplitude falls below a certain threshold, the vertical velocity is too weak to generate the convection necessary to initiate the growth process seen in the control simulation. Interestingly, growth rates from horizontal shear are not substantially different among the three experiments, while the growth rate from pressure work falls by a factor of two as the initial amplitude is halved (Figure 13c). This suggests that the synoptic-scale wave structure is acting independently from the convection. The results of Experiment C demonstrate that the growth process simulated here requires an initial disturbance of sufficient amplitude. In the real atmosphere, this points to the importance of a predecessor disturbance from upstream (e.g., Chen and Weng, 1999) or some initial convectively generated vortex to start the growth process.

### 3.3.4 | Friction (Experiment D)

In our final set of experiments (Experiment D), we examine the sensitivity to friction. As noted in the introduction, a number of studies have cited CISK as an important growth process for monsoon depressions. We test its importance in our simulation by deactivating surface friction, that is, setting  $C_E$  in Equation 8 to zero. This modification tests only the version of CISK that requires frictional convergence in the boundary layer to force ascent and convection, and not the version that links this convergence to a wave mode (i.e., wave-CISK). Also recall that, similarly to the experiment that altered surface heat and moisture fluxes, we are altering only the perturbation friction. Results are shown in Figure 11d. Judging by the –18 hPa pressure perturbation achieved by the disturbance without friction, convergence induced by friction

does not appear to be an essential part of the growth mechanism. Interestingly, energy lost through numerical diffusion increases substantially in this experiment, with the turbulence parametrization reduced to a secondary energy sink (Figure 12d). This indicates that a larger portion of the perturbation kinetic energy is concentrated near the grid scale, where numerical diffusion acts most strongly. A possible explanation is that, without friction to reduce surface winds, substantial grid-scale noise develops. Nevertheless, there is some evidence that the lack of frictional convergence at the surface does lead to proportionately less disturbance growth through latent heat release: despite the minimum pressure being substantially lower than in the control, the growth rate from pressure work is smaller (Figure 13d). The fact that the total energy gained from pressure work is nearly the same between the two experiments (Figure 12d) is more a reflection of the much larger amplitude of the disturbance in the frictionless case. Cross-referencing plots of the rain field (not shown), the disturbance is somewhat less convectively active, especially near the circulation center, where surface convergence forced by boundary-layer friction should be largest.

In the final part of Experiment D, we double the friction coefficient in Equation 8 over land in order to test the extent to which increased friction over land leads to the disturbance's demise. Note that, even in the control simulation, friction over land is specified to be higher than it is over water. As seen in Figure 11d, this modification reduces the amplitude of the low pressure slightly after day 6, which is near landfall. This suggests that, at least in this simulation, the increase in friction over land has a small impact on disturbance decay. This is further supported by the fact that, even without friction, the disturbance begins to weaken at approximately the same time.

## 4 | SUMMARY AND DISCUSSION

The experiments presented here suggest that monsoon depressions are a type of moist barotropic instability. For a dry atmosphere, a basic state constructed from observations of the South Asian monsoon supports stable Rossby-wave-like disturbances that draw energy from the meridional shear of the basic state and resemble monsoon depressions (Diaz and Boos, 2019). Being stable, these waves cannot appear spontaneously, but rather require some preexisting disturbance of sufficient amplitude. With the addition of moisture, the pattern of vertical motion induced by their interaction with basic-state gradients of wind, temperature, and vorticity couples them with condensation. This coupling amplifies the otherwise decaying disturbance. Although the condensation is offset from the circulation center, the combined flow of the vortex and large-scale monsoon enables potential vorticity generated by this condensation to remain colocated with the larger-scale vortex as it spirals around the circulation center. This contrasts with theories of moist baroclinic

instability, which require disturbances to tilt upshear in the latitude–height plane in order to bring the diabatic potential vorticity (PV) generation in phase with positive PV anomalies. It also contrasts with the moisture-vortex instability of Adames and Ming (2018a), which relies on a convective time delay to bring the PV generation in phase with the PV anomalies. In summary, the least stable normal mode of the basic state explains the structure and synoptic-scale size of the monsoon depression, while coupling with moist convection takes this system from weakly stable to unstable.

Although we refer to disturbance growth in our simulations as moist barotropic instability, a distinction must be made between this mechanism and that explored by Lambaerts *et al.* (2011), which is arguably a more pure form of moist barotropic instability. In their case, precipitation is generated by the ageostrophic response to the barotropic instability itself. In our case, we argue that strong vertical shear and gradients of temperature and vorticity interact with the vortex to generate the ageostrophic flow that causes precipitation. Thus, even though the environmental baroclinicity does not seem to contribute to growth through a classic baroclinic instability, it may be essential for producing the distribution of vertical velocity necessary to couple this disturbance to convection.

Though theoretical work on moist barotropic instability is limited (Kuo, 1978; Lambaerts *et al.*, 2011), the mechanism presented above bears some resemblance to explanations for the amplification of easterly waves, which, similarly to monsoon depressions, occasionally evolve into tropical cyclones. For example, African easterly waves draw energy from the meridional shear of the background flow and are coupled to convection (Kiladis *et al.*, 2006). This coupling has been explained using the QG-omega equation (Kiladis *et al.*, 2006) and some have argued that it is essential for wave growth (Berry and Thorncroft, 2012). Rydbeck and Maloney (2015) have made similar arguments for easterly waves in the eastern Pacific, with the additional proposal that convection forces the wave axis to elongate from southwest to northeast, a configuration needed to draw energy from the meridional shear. These views of moist barotropic instability contrast with that of Schubert *et al.* (1991), which focuses on how convection alters the basic state itself, though it is possible that this process is also relevant to monsoon depressions.

Our explanation of how convection interacts with the monsoon depression vortex has parallels with the “marsupial paradigm” of tropical cyclogenesis introduced by Dunkerton *et al.* (2009). According to that theory, the region where an easterly wave trough intersects its critical latitude favors tropical cyclogenesis due to the presence of a metaphorical “pouch”, a region of strong rotation, higher inertial stability, and flow stagnation. For our basic state, since the slowest-decaying normal mode moves slowly westward, it would have a critical latitude (defined as the location where

wave-relative flow goes to zero) just north of the zero-wind line. In our simulations, convection occurs close enough to this region that its generated vorticity can be recirculated rather than differentially advected by the strong basic-state meridional and vertical shear. Thus, this particular theory of tropical cyclogenesis could be relevant to monsoon depression genesis. As suggested by the IMD ranking system, perhaps monsoon depressions represent an early phase of tropical cyclogenesis that is ultimately inhibited by vertical wind shear. In fact, when we remove the basic-state fields in our simulation abruptly while the disturbance is amplifying, it becomes much stronger, as it undergoes tropical cyclogenesis and the WISHE mechanism begins to operate. Thus, once the monsoon depression reaches a certain amplitude, the basic state which nurtured its growth may become detrimental, presumably owing to the high vertical wind shear.

Our results suggest that the WISHE mechanism is not necessary for the formation of monsoon depressions: even with anomalous surface heat and moisture fluxes eliminated, the simulated disturbance amplifies at nearly the same rate and reaches a similar minimum pressure. Nevertheless, without these fluxes, the disturbance weakens faster after reaching its maximum intensity, suggesting that surface heat and moisture fluxes do become an important energy source once it reaches sufficient amplitude. This result should not be interpreted as suggesting that warm water is not favorable for monsoon depression genesis. The formulation of our equations requires an implicit surface moisture flux to maintain the basic-state moisture field, and this moisture ultimately originated from the ocean. Indeed, statistical analysis showed that monsoon depressions form more frequently where the climatological surface moist energy content is elevated relative to that of the upper troposphere (Ditchek *et al.*, 2016), extending ideas of the importance of “relative SST” (Vecchi and Soden, 2007) and tropical cyclone potential intensity (Emanuel, 1988) to monsoon depressions. Our results only suggest that a WISHE-like feedback between the surface wind speed of the amplifying vortex and the surface heat and moisture flux is not essential. It should also be noted that some have argued that WISHE may not always be important in the early phase of tropical cyclogenesis and that a moderate amount of wind shear at this early stage could be beneficial, by enhancing convection (Molinari *et al.*, 2004).

Additionally, our results do not support frictionally driven CISK being an essential growth process; turning off surface friction resulted in a substantially stronger vortex in our experiments, presumably because friction is an energy sink. However, considering that the growth rate from pressure work was smaller in the no-friction simulation compared with the control, frictional convergence likely makes some contribution to enhancing convection, even if it is not the leading factor. Although we argue that this disturbance has Rossby-wave-like properties, the classical wave-CISK

paradigm also does not seem applicable, since it is usually framed in terms of equatorial wave modes (Lindzen, 1974).

An important caveat is that we did not explore the sensitivity of our results to the basic state. The South Asian monsoon environment varies substantially with time and our simulations used only one possible state, albeit one that we aimed to make as relevant as possible to monsoon depressions. Other basic states might support different ratios of the aforementioned growth mechanisms or different ones entirely. Storm systems in this region might exist on a continuum from more monsoon-depression-like, as in the one we have simulated, to more tropical-cyclone-like.

## ACKNOWLEDGEMENTS

This work was supported by the U.S. Department of Energy, Office of Science, Biological and Environmental Research under award DE-SC0019367, and by the National Science Foundation under award AGS-1746160. Model integrations used the Savio computational cluster, provided by Berkeley Research Computing at the University of California, Berkeley.

## ORCID

Michael Diaz  <https://orcid.org/0000-0002-0442-3583>

William R. Boos  <https://orcid.org/0000-0001-9076-3551>

## REFERENCES

- Adames, Á.F. and Ming, Y. (2018a) Interactions between water vapor and potential vorticity in synoptic-scale monsoonal disturbances: moisture vortex instability. *Journal of the Atmospheric Sciences*, 75(6), 2083–2105.
- Adames, Á.F. and Ming, Y. (2018b) Moisture and moist static energy budgets of South Asian monsoon low pressure systems in GFDL AM4.0. *Journal of the Atmospheric Sciences*, 75(6), 2107–2123.
- Anthes, R.A. (1970) Numerical experiments with a two-dimensional horizontal variable grid. *Monthly Weather Review*, 98(11), 810–822.
- Aravequia, J., Brahmananda Rao, V. and Bonatti, J. (1995) The role of moist baroclinic instability in the growth and structure of monsoon depressions. *Journal of the Atmospheric Sciences*, 52(24), 4393–4409.
- Berry, G.J. and Thorncroft, C.D. (2012) African easterly wave dynamics in a mesoscale numerical model: the upscale role of convection. *Journal of the Atmospheric Sciences*, 69(4), 1267–1283.
- Boos, W., Hurley, J. and Murthy, V. (2015) Adiabatic westward drift of Indian monsoon depressions. *Quarterly Journal of the Royal Meteorological Society*, 141(689), 1035–1048.
- Boos, W.R., Mapes, B.E. and Murthy, V.S. (2017) Potential vorticity structure and propagation mechanism of Indian monsoon depressions. In: Chang, C.-P., Kuo, H.-C., Lau, N.-C., Johnson, R.H., Wang, B. and Wheeler, M.C. (Eds.) *The Global Monsoon System: Research and Forecast*. Singapore: World Scientific, pp. 187–199.

- Bretherton, C.S. (2003) Wave-CISK. In: Holton, J.R., Curry, J.A. and Pyle, J.A. (Eds.) *Encyclopedia of Atmospheric Sciences*. Amsterdam: Academic Press, pp. 1019–1021.
- Camargo, S.J., Emanuel, K.A. and Sobel, A.H. (2007) Use of a genesis potential index to diagnose ENSO effects on tropical cyclone genesis. *Journal of Climate*, 20(19), 4819–4834.
- Charney, J.G. and Eliassen, A. (1964) On the growth of the hurricane depression. *Journal of the Atmospheric Sciences*, 21(1), 68–75.
- Chen, T.C. and Weng, S.P. (1999) Interannual and intraseasonal variations in monsoon depressions and their westward-propagating predecessors. *Monthly Weather Review*, 127(6), 1005–1020.
- Chen, T.C. and Yoon, J.H. (2000) Some remarks on the westward propagation of the monsoon depression. *Tellus A*, 52(5), 487–499.
- Chen, T.C., Yoon, J.H. and Wang, S.Y. (2005) Westward propagation of the Indian monsoon depression. *Tellus A*, 57(5), 758–769.
- Cohen, N.Y. and Boos, W.R. (2016) Perspectives on moist baroclinic instability: implications for the growth of monsoon depressions. *Journal of the Atmospheric Sciences*, 73(4), 1767–1788.
- Crum, F.X. and Dunkerton, T.J. (1992) Analytic and numerical models of wave-CISK with conditional heating. *Journal of the Atmospheric Sciences*, 49(18), 1693–1708.
- Daggupati, S.M. and Sikka, D.R. (1977) On the vorticity budget and vertical velocity distribution associated with the life cycle of a monsoon depression. *Journal of the Atmospheric Sciences*, 34(5), 773–792.
- Dash, S., Kumar, J.R. and Shekhar, M. (2004) On the decreasing frequency of monsoon depressions over the Indian region. *Current Science*, 86, 1404–1411.
- Dee, D.P., Uppala, S.M., Simmons, A.J., Berrisford, P., Poli, P., Kobayashi, S., Andrae, U., Balmaseda, M.A., Balsamo, G., Bauer, P., Bechtold, P., Beljaars, A.C.M., van de Berg, L., Bidlot, J., Bormann, N., Delsol, C., Dragani, R., Fuentes, M., Geer, A.J., Haimberger, L., Healy, S.B., Hersbach, H., Holm, E.V., Isaksen, I., Kallberg, P., Kohler, M., Maricardi, M., McNally, A.P., Monge-Sanz, B.M., Morcrette, J.J., Park, B.K., Peubey, C., de Rosnay, P., Tavolato, C., Thepaut, J.N. and Vitart, F. (2011) The ERA-Interim reanalysis: configuration and performance of the data assimilation system. *Quarterly Journal of the Royal Meteorological Society*, 137(656), 553–597.
- Diaz, M. and Boos, W.R. (2019) Barotropic growth of monsoon depressions. *Quarterly Journal of the Royal Meteorological Society*, 145(719), 824–844.
- Ditchek, S.D., Boos, W.R., Camargo, S.J. and Tippett, M.K. (2016) A genesis index for monsoon disturbances. *Journal of Climate*, 29(14), 5189–5203.
- Dunkerton, T., Montgomery, M. and Wang, Z. (2009) Tropical cyclogenesis in a tropical wave critical layer: easterly waves. *Atmospheric Chemistry and Physics*, 9(15), 5587–5646.
- Emanuel, K. and Nolan, D.S. (2004). Tropical cyclone activity and the global climate system. In: *26th Conference on Hurricanes and Tropical Meteorology May 2004*. Miami, FL: American Meteorological Society, pp. 240–241
- Emanuel, K.A. (1986) An air–sea interaction theory for tropical cyclones. Part I: steady-state maintenance. *Journal of the Atmospheric Sciences*, 43(6), 585–605.
- Emanuel, K.A. (1988) The maximum intensity of hurricanes. *Journal of the Atmospheric Sciences*, 45(7), 1143–1155.
- Godbole, R.V. (1977) The composite structure of the monsoon depression. *Tellus*, 29(1), 25–40.
- Goswami, B., Keshavamurty, R. and Satyan, V. (1980) Role of barotropic, baroclinic and combined barotropic-baroclinic instability for the growth of monsoon depressions and mid-tropospheric cyclones. *Proceedings of the Indian Academy of Sciences—Earth and Planetary Sciences*, 89(1), 79–97.
- Hoskins, B. (1997) A potential vorticity view of synoptic development. *Meteorological Applications*, 4(4), 325–334.
- Hoskins, B., Draghici, I. and Davies, H. (1978) A new look at the  $\omega$ -equation. *Quarterly Journal of the Royal Meteorological Society*, 104(439), 31–38.
- Hoskins, B.J., McIntyre, M. and Robertson, A.W. (1985) On the use and significance of isentropic potential vorticity maps. *Quarterly Journal of the Royal Meteorological Society*, 111(470), 877–946.
- Hunt, K.M. and Turner, A.G. (2017a) The effect of horizontal resolution on Indian monsoon depressions in the Met Office NWP model. *Quarterly Journal of the Royal Meteorological Society*, 143(705), 1756–1771.
- Hunt, K.M. and Turner, A.G. (2017b) The effect of soil moisture perturbations on Indian monsoon depressions in a numerical weather prediction model. *Journal of Climate*, 30(21), 8811–8823.
- Hunt, K.M., Turner, A.G., Inness, P.M., Parker, D.E. and Levine, R.C. (2016) On the structure and dynamics of Indian monsoon depressions. *Monthly Weather Review*, 144(9), 3391–3416.
- Hurley, J.V. and Boos, W.R. (2015) A global climatology of monsoon low-pressure systems. *Quarterly Journal of the Royal Meteorological Society*, 141(689), 1049–1064.
- Kasture, S., Keshavamurty, R. and Satyan, V. (1993) A model study of the growth of summer monsoon disturbances. *Current Science*, 64(9), 673–679.
- Keshavamurty, R., Asnani, G., Pillai, P. and Das, S. (1978) Some studies of the growth of monsoon disturbances. *Proceedings of the Indian Academy of Sciences—Section A, Earth and Planetary Sciences*, 87(3), 61–75.
- Kessler, E. (1969) On the distribution and continuity of water substance in atmospheric circulations. *On the Distribution and Continuity of Water Substance in Atmospheric Circulations*. Boston, MA: American Meteorological Society, pp. 1–84.
- Kiladis, G.N., Thorncroft, C.D. and Hall, N.M. (2006) Three-dimensional structure and dynamics of African easterly waves. Part I: observations. *Journal of the Atmospheric Sciences*, 63(9), 2212–2230.
- Krishnakumar, V., Keshavamurty, R. and Kasture, S. (1992) Moist baroclinic instability and the growth of monsoon depressions—linear and nonlinear studies. *Proceedings of the Indian Academy of Sciences—Earth and Planetary Sciences*, 101(2), 123–152.
- Krishnamurti, T., Kanamitsu, M., Godbole, R., Chang, C.B., Carr, F. and Chow, J.H. (1976) Study of a monsoon depression (II), dynamical structure. *Journal of the Meteorological Society of Japan. Ser. II*, 54(4), 208–225.
- Krishnamurti, T., Martin, A., Krishnamurti, R., Simon, A., Thomas, A. and Kumar, V. (2013) Impacts of enhanced CCN on the organization of convection and recent reduced counts of monsoon depressions. *Climate Dynamics*, 41(1), 117–134.
- Krishnan, R., Ayantika, D., Kumar, V. and Pokhrel, S. (2011) The long-lived monsoon depressions of 2006 and their linkage with the Indian Ocean Dipole. *International Journal of Climatology*, 31(9), 1334–1352.
- Kuo, H. (1978) A two-layer model study of the combined barotropic and baroclinic instability in the Tropics. *Journal of the Atmospheric Sciences*, 35(10), 1840–1860.

- Lambaerts, J., Lapeyre, G. and Zeitlin, V. (2011) Moist versus dry barotropic instability in a shallow-water model of the atmosphere with moist convection. *Journal of the Atmospheric Sciences*, 68(6), 1234–1252.
- Lambaerts, J., Lapeyre, G. and Zeitlin, V. (2012) Moist versus dry baroclinic instability in a simplified two-layer atmospheric model with condensation and latent heat release. *Journal of the Atmospheric Sciences*, 69(4), 1405–1426.
- Lindzen, R., Farrell, B. and Rosenthal, A. (1983) Absolute barotropic instability and monsoon depressions. *Journal of the Atmospheric Sciences*, 40(5), 1178–1184.
- Lindzen, R.S. (1974) Wave-CISK in the Tropics. *Journal of the Atmospheric Sciences*, 31(1), 156–179.
- Mishra, S. (2018) On the evolution of planetary-scale fields and genesis of monsoon depressions over the Indian region. *Quarterly Journal of the Royal Meteorological Society*, 144(710), 129–141.
- Molinari, J., Vollaro, D. and Corbosiero, K.L. (2004) Tropical cyclone formation in a sheared environment: a case study. *Journal of the Atmospheric Sciences*, 61(21), 2493–2509.
- Moorthi, S. and Arakawa, A. (1985) Baroclinic instability with cumulus heating. *Journal of the Atmospheric Sciences*, 42(19), 2007–2031.
- Nitta, T. and Masuda, K. (1981) Observational study of a monsoon depression developed over the Bay of Bengal during summer MONEX. *Journal of the Meteorological Society of Japan. Ser. II*, 59(5), 672–682.
- Prajeesh, A., Ashok, K. and Rao, D.B. (2013) Falling monsoon depression frequency: a Gray–Sikka conditions perspective. *Scientific Reports*, 3, 2989.
- Rajamani, S. and Rao, K. (1981) On the occurrence of rainfall over southwest sector of monsoon depression. *Mausam*, 32, 215–220.
- Rao, K. and Rajamani, S. (1970) Diagnostic study of a monsoon depression by geostrophic baroclinic model. *Indian Journal of Meteorology and Geophysics*, 21, 187–194.
- Rotunno, R. and Emanuel, K.A. (1987) An air–sea interaction theory for tropical cyclones. Part II: evolutionary study using a nonhydrostatic axisymmetric numerical model. *Journal of the Atmospheric Sciences*, 44(3), 542–561.
- Rydbeck, A.V. and Maloney, E.D. (2015) On the convective coupling and moisture organization of east Pacific easterly waves. *Journal of the Atmospheric Sciences*, 72(10), 3850–3870.
- Sanders, F. (1984) Quasi-geostrophic diagnosis of the monsoon depression of 5–8 July 1979. *Journal of the Atmospheric Sciences*, 41(4), 538–552.
- Schubert, W.H., Ciesielski, P.E., Stevens, D.E. and Kuo, H.C. (1991) Potential vorticity modeling of the ITCZ and the Hadley circulation. *Journal of the Atmospheric Sciences*, 48(12), 1493–1509.
- Shukla, J. (1978) CISK–barotropic–baroclinic instability and the growth of monsoon depressions. *Journal of the Atmospheric Sciences*, 35(3), 495–508.
- Sikka, D. (1977) Some aspects of the life history, structure and movement of monsoon depressions. *Pure and Applied Geophysics*, 115, 1501–1529.
- Skamarock, W.C., Klemp, J.B., Dudhia, J., Gill, D.O., Barker, D.M., Wang, W. and Powers, J.G. (2008) A description of the advanced research WRF version 3. NCAR Technical Note –475+STR. Boulder, CO: NCAR.
- Sobel, A.H., Nilsson, J. and Polvani, L.M. (2001) The weak temperature gradient approximation and balanced tropical moisture waves. *Journal of the Atmospheric Sciences*, 58(23), 3650–3665.
- Sørland, S.L. and Sorteberg, A. (2015) The dynamic and thermodynamic structure of monsoon low-pressure systems during extreme rainfall events. *Tellus A: Dynamic Meteorology and Oceanography*, 67(1), 27 039.
- Sørland, S.L., Sorteberg, A., Liu, C. and Rasmussen, R. (2016) Precipitation response of monsoon low-pressure systems to an idealized uniform temperature increase. *Journal of Geophysical Research: Atmospheres*, 121(11), 6258–6272.
- Subrahmanyam, D., Tandon, M., George, L. and Mishra, S. (1981) Role of barotropic mechanism in the development of a monsoon depression: a MONEX study. *Pure and Applied Geophysics*, 119(5), 901–912.
- Thorncroft, C. and Hoskins, B. (1994) An idealized study of African easterly waves. II: a nonlinear view. *Quarterly Journal of the Royal Meteorological Society*, 120(518), 983–1015.
- Tippett, M.K., Camargo, S.J. and Sobel, A.H. (2011) A poisson regression index for tropical cyclone genesis and the role of large-scale vorticity in genesis. *Journal of Climate*, 24(9), 2335–2357.
- Vecchi, G.A. and Soden, B.J. (2007) Increased tropical Atlantic wind shear in model projections of global warming. *Geophysical Research Letters*, 34(8), 1–5.
- Vishnu, S., Francis, P., Shenoi, S. and Ramakrishna, S. (2016) On the decreasing trend of the number of monsoon depressions in the Bay of Bengal. *Environmental Research Letters*, 11(1), 014 011.
- Vishnu, S., Francis, P.A., Shenoi, S.C. and Ramakrishna, S.S.V.S. (2018) On the relationship between the Pacific Decadal Oscillation and monsoon depressions over the Bay of Bengal. *Atmospheric Science Letters*, 19(7), e825.
- Weisman, M.L., Skamarock, W.C. and Klemp, J.B. (1997) The resolution dependence of explicitly modeled convective systems. *Monthly Weather Review*, 125(4), 527–548.

**How to cite this article:** Diaz M, Boos WR. Monsoon depression amplification by moist barotropic instability in a vertically sheared environment. *QJR Meteorol Soc.* 2019;145:2666–2684. <https://doi.org/10.1002/qj.3585>